Hydrogen-vacancy complexes in electron-irradiated niobium

Jakub Čížek,* Ivan Procházka, and Stanislav Daniš
Faculty of Mathematics and Physics, Charles University in Prague, V Holešovičkách 2, CZ-18000 Praha 8, Czech Republic

Gerhard Brauer and Wolfgang Anwand
Institut für Ionenstrahlphysik und Materialforschung, Forschungszentrum Dresden-Rossendorf, Postfach 510119, D-01314 Dresden, Germany

Ryota Gemma, Eugen Nikitin, Reiner Kirchheim, and Astrid Pundt
Institut für Materialphysik, Universtät Göttingen, Friedrich-Hund Platz 1, D-37073 Göttingen, Germany

Rinat K. Islamgaliev
Institute of Physics of Advanced Materials, Ufa State Aviation Technical University, 12 K. Marx Street, 450000 Ufa, Russian Federation
(Received 22 November 2008; revised manuscript received 28 December 2008; published 17 February 2009)

The aim of the present work was to investigate the microstructure of bulk niobium irradiated by 10 MeV electrons. Positron-annihilation spectroscopy was employed as a principal technique for the characterization of irradiation-induced defects. Experimental results were compared to first-principles theoretical calculations of positron characteristics. In addition to extended positron-annihilation studies, the specimens were characterized also by x-ray diffraction. It was found that irradiation-induced vacancies are surrounded by hydrogen. Complexes consisting of a Nb vacancy surrounded by one and two H atoms were identified in the irradiated specimens. The concentration of these vacancy-hydrogen complexes was estimated to be $(18-24)\times10^{-5}$ at. %. Vacancy-2H complexes are found to represent the dominating type of defects. Hydrogen atoms surrounding a Nb vacancy cause a shortening of the lifetime of trapped positrons. Moreover, it was demonstrated that hydrogen attached to Nb vacancy can be identified by coincidence Doppler broadening technique. The effect of a thin Pd (or Cr) overlayer on the irradiation-induced defects was investigated also. It was found that the relative fraction of vacancy-2H complexes is higher in the specimens irradiated with such an overlayer.

DOI: 10.1103/PhysRevB.79.054108 PACS number(s): 78.70.Bj, 61.72.−y

I. INTRODUCTION

Niobium is an important material for high-temperature technology and for advanced fission and fusion reactors. Moreover, it is used for superconductive rf cavities in particle accelerators. The information about irradiation-induced defects in Nb is highly important for the above-mentioned applications. In addition, Nb is known to absorb hydrogen easily.[1] Moreover, hydrogen in Nb exhibits a high mobility even at low temperatures (~60 K).[2,3] This makes the characterization of irradiated specimens more complicated because one has to consider the interaction of defects created by irradiation with hydrogen absorbed in Nb. For this reason, it is very important to learn more about the mechanism of interaction between hydrogen and irradiation-induced lattice defects. In general, the knowledge about hydrogen interaction with defects in metals is still limited despite an increasing effort given to such investigations, especially on the atomic scale [see the recent review (Ref. 4) for more information].

Positron-annihilation spectroscopy (PAS) is a well established nondestructive method with very high sensitivity to vacancies and other open-volume defects.[5] It has proven itself to be a very powerful tool for investigations of hydrogen interaction with defects in metals on the atomic scale. For example, hydrogen trapping at vacancies in Cu was experimentally demonstrated by Lengeler *et al.*[6] by means of PAS almost 30 years ago.

Hautojärvi and co-workers[7,8] employed PAS for investigations of vacancy recovery in Nb irradiated by 3 MeV electrons at liquid nitrogen temperature. The authors found that a Nb specimen, which was handled in a protective He atmosphere in order to prevent it from hydrogen contamination, exhibits a lifetime of irradiation-induced defects of (210 ± 2) ps, while the sample kept in air exhibits the lifetime (170 ± 2) ps. In addition, the migration of the irradiation-induced defects occurred already at 220 K in the sample handled under the protective atmosphere, but it was shifted to 380 K in the sample kept on air. The authors explained these experimental findings by hydrogen trapping at irradiation-induced vacancies in the Nb sample kept on air. Hydrogen attached to a vacancy causes a decrease of lifetime of trapped positrons. It may also decrease the mobility of a vacancy, i.e., to stabilize it. Thus, it is assumed that the sample handled in a protective He atmosphere is virtually hydrogen free and contains nondecorated Nb vacancies which are annealed out already below room temperature. On the other hand, the sample kept on air contains vacancy-hydrogen complexes which are stable up to 380 K. Theoretical calculations performed in Ref. 8 suggested that the latter sample contains most probably a mixture of vacancies associated either with one H atom (v-H) or with 2 H atoms (v-2H).

In the present work, we continue with the investigations of hydrogen interaction with defects in electron-irradiated Nb and extend them in several respects:

(i) For a precise characterization of the irradiation-induced defects and their coupling with hydrogen, high-resolution positron lifetime (LT) spectroscopy is employed,

with a timing resolution more than two times better than mentioned in Ref. 8. Moreover, a relatively high coincidence count rate allows to accumulate a high statistics ($>10^7$) in the LT spectra at reasonable time. An excellent timing resolution and a high statistics enable to distinguish even components with closely spaced lifetimes, i.e., those expected for vacancies surrounded by various numbers of H atoms.

(ii) Coincidence Doppler broadening (CDB) is employed for an investigation of the chemical surrounding of electron-irradiation-induced Nb vacancies. The experimental high-momentum profiles (HMP) are compared to theoretical modeling.

(iii) Defect depth profiles are studied by slow positron implantation spectroscopy (SPIS).

(iv) The effect of a thin Pd (and Cr) overlayer of the specimen on the irradiation-induced vacancy-hydrogen complexes is investigated.

The paper is structured as follows. Experimental details are given in Sec. II. Theoretical modeling of defects is described in Sec. III. Characterization of virgin Nb samples can be found in Sec. IV A, while Sec. IV B describes defects in the electron-irradiated specimens. Section IV E describes further treatment of experimental data and an estimation of defect concentrations. The CDB experimental results and calculated HMP curves are presented in Sec. IV F. Final conclusions are drawn in Sec. V.

II. EXPERIMENT

A. Specimens

Bulk Nb (99.9%) specimens (disk shaped, diameter $\approx$10 mm, thickness $\approx$0.5 mm) were first annealed (1000 °C/1 h) in vacuum (10^{-3} mbar) to remove virtually all defects introduced during casting and shaping. The specimens were subsequently irradiated with 10 MeV electrons up to a fluence of 2×10^{21} m^{-2} ($T_{irr}\leq100$ °C). The surface of the specimens was covered with a 30 nm thick Pd overlayer deposited by cold cathode beam sputtering in an UHV chamber (10^{-10} mbar). Specimens with a Pd cap sputtered *prior to* electron irradiation were compared to those having a Pd cap deposited *after* irradiation. Another set of specimens was covered prior to irradiation with a 30 nm Cr overlayer instead of the Pd cap.

After characterization of the irradiated state, the specimen irradiated with Pd cap was subsequently doped with hydrogen. Hydrogen loading was performed by cathodic electrochemical charging on the setup described in our previous paper.[9] A mixture of H_3PO_4(80%) and glycerin (80%) in 1:1 ratio was used as electrolyte. Hydrogen charging was made by applying constant current of 0.3 mA for 17 h.

Another set of annealed specimens was subjected to severe plastic deformation in order to create a high density of dislocations. The samples were deformed by torsion and simultaneously compressed by a high pressure of 6 GPa. This technique of severe plastic deformation is called high-pressure torsion (HPT) (Ref. 10) and enables one to achieve ultrafine-grained structure with a high density of dislocations. Specimens deformed by HPT were used as reference for interpretation of CDB curves in Sec. IV F.

B. PAS

A $^{22}Na_2CO_3$ positron source (1.5 MBq) deposited on a 2 μm thick Mylar foil was used in LT and CDB measurements. This source was always forming a sandwich with two identically treated Nb specimens. The source contribution in LT spectra consisted of two weak components with lifetimes $\approx$368 ps and $\approx$1.5 ns and corresponding intensities of $\approx$8% and $\approx$1%, respectively. LT spectroscopy was performed using a fast-fast spectrometer[11,12] with a timing resolution of 160 ps (full width at half maximum, FWHM ^{22}Na). At least 10^7 positron-annihilation events were accumulated at each LT spectrum which was subsequently decomposed using a maximum-likelihood procedure.[13]

CDB studies were carried out on a spectrometer[14] equipped with two high purity germanium (HPGe) detectors. The energy resolution of the CDB spectrometer was 1.02 keV at 511 keV. At least 10^8 annihilation events were collected in each two-dimensional γ-ray energy spectrum.

SPIS studies were performed at the magnetically guided positron beam "SPONSOR" (Ref. 15) with positron energy E adjustable from 0.03 to 36 keV. Doppler broadening of the annihilation line was measured by a HPGe detector with an energy resolution of 1.09 keV at 511 keV and evaluated using the S and W line-shape parameters. The $S(E)$ dependencies were fitted by the VEPFIT software package.[16] It has to be noted that all the S and W parameters shown in this paper were normalized to the bulk values S_0, W_0 measured on the annealed Nb specimen.

C. X-ray diffraction

X-ray diffraction (XRD) measurements were taken in $\Theta/2\Theta$ geometry with Philips X'pert MPD diffractometers using Cu K_α radiation. The XRD profiles were fitted with the Pearson VII function, and the lattice parameters were determined by the Cohen-Wagner extrapolation plot (a_{hkl} vs $\cos\Theta\cot\Theta$).

III. THEORY

A. Theoretical calculations of positron parameters

Positron properties were calculated using density-functional theory (DFT) in so-called zero positron density limit.[17] In this approximation positron density is assumed to be everywhere vanishingly small and not affecting the bulk electron structure. The positron and its screening electron cloud are considered to form a neutral quasiparticle. At first electron density $n(\mathbf{r})$ is solved without the positron. Subsequently, the effective potential for positron is constructed as

$$V_+(\mathbf{r}) = \phi(\mathbf{r}) + V_{corr}[n(\mathbf{r})], \quad (1)$$

where $\phi(\mathbf{r})$ is the Coulomb potential produced by the charge distribution of electrons and nuclei and $V_{corr}[n(\mathbf{r})]$ is the zero positron density limit of the electron-positron correlation potential.[18] This so-called "conventional scheme" has been widely used for calculations of positron parameters in various solid systems (see, e.g., Ref. 17) and the agreement of the calculated parameters with experiment is usually better than 10%.

TABLE I. Calculated Nb bulk positron lifetimes τ_B and lifetimes of positrons trapped in Nb vacancy. The lifetimes collected in the table were calculated using superimposed atomic electron densities (ATSUP) or self-consistent electron density (VASP) combined with LDA and GGA approaches for electron-positron correlation. Positron lifetimes calculated in Refs. 26 and 29 using the LMTO method within the ASA and GGA schemes are shown for comparison. Experimental positron lifetimes are listed in the last column.

	ATSUP-LDA	ATSUP-GGA	VASP-LDA	VASP-GGA	LMTO(ASA)-GGA	Experiment
Bulk τ_B (ps)	125.9	134.4	116.9	120.1	122[a]	128.3 ± 0.4
					122[b]	122 ± 2 [c]
Vacancy τ_v (ps)	222.7	223.9	205.0	210.6	218[a]	210 ± 2 [c]
					220[b]	
$\frac{\tau_B}{\tau_v}$	1.77	1.67	1.75	1.75	1.79[a]	1.72–1.64
					1.80[b]	

[a]Reference 26.
[b]Reference 29.
[c]Reference 8.

Electron density needed for construction of the effective positron potential was calculated using two approaches:

(i) Atomic superposition (ATSUP) method[19] which uses superimposed atomic electron densities calculated by a self-consistent relativistic atomic code.[20,21] ATSUP approach uses non-self-consistent electron density and neglects charge transfer, but it is a very fast method which can be used even for very large supercells.

(ii) Self-consistent valence electron density was calculated by the plane-wave code Vienna *ab initio* simulation package (VASP).[22–24] In this approach frozen-core electron orbitals were added to the self-consistent VASP valence electron density. The $4d^4$, $5s^1$ Nb electrons and $1s^1$ H electron were considered as valence electrons in VASP calculations.

Two approaches were used also for the correlation part of the positron potential:

(i) local-density approximation (LDA) using results of Arponen and Pajane[25] parametrized by Boroński and Nieminen,[18] and

(ii) generalized gradient scheme (GGA) formulated by Barbiellini *et al.*[26]

Thus, a combination of the approaches described above results in four various schemes how to calculate positron parameters denoted here: ATSUP-LDA, ATSUP-GGA, VASP-LDA, and VASP-GGA.

Positron wave functions $\psi_i^+(\mathbf{r})$ are calculated by solution of a single-particle Schrodinger equation

$$-\frac{1}{2}\nabla^2\psi_i^+(\mathbf{r}) + V_+(\mathbf{r})\psi_i^+(\mathbf{r}) = \epsilon_i\psi_i^+(\mathbf{r}). \quad (2)$$

The positron-annihilation rate (i.e., the inverse of positron lifetime) is determined using the expression

$$\lambda = \pi r_e^2 c \int |\psi^+(\mathbf{r})|^2 n(\mathbf{r})\gamma[n(\mathbf{r})]d\mathbf{r}, \quad (3)$$

where r_e is the classical electron radius, c is the speed of light, and $\gamma[n(\mathbf{r})]$ denotes the electron enhancement factor describing the pileup of electrons at the positron site.[17] In LDA approach the enhancement factor depends only on local electron density on the positron site. Here we used parametrization of the enhancement factor introduced by Boroński and Nieminen.[18] The GGA enhancement factor at a given point depends both on the electron density at the positron site and also on its gradient.[26,27] In GGA calculations we used the enhancement factor based on Arponen and Pajanne[25] results with gradient correction constructed by Barbiellini *et al.*[26] The adjustable parameter $\alpha=0.22$ (see Ref. 26) was applied for the enhancement factor in GGA calculations.

The ATSUP calculations were performed on $4\times4\times4$ supercells containing 128 Nb atoms. One Nb atom was removed for modeling a vacancy and corresponding H atoms were added for calculations of vacancy-hydrogen complexes. Integration over the Brillouin zone described in Ref. 28 was used in calculations of positron parameters for vacancy and vacancy-hydrogen complexes. Investigations regarding the convergence of calculated positron parameters with respect to the supercell sizes performed in Ref. 28 have shown that supercells used in the present calculations can be considered as sufficiently large for calculations of positrons trapped in vacancy. Indeed, positron parameters which were calculated for selected configurations on $5\times5\times5$ (250 Nb atoms) supercell show virtually no difference from those calculated on 128 Nb atom-based supercells.

VASP calculations were performed on $3\times3\times3$ (54 atom-based) supercells using $5\times5\times5$ k-point mesh. Virtually the same results within a relative difference of 1% were obtained using larger $4\times4\times4$ (128 atom-based) supercells with coarser k-point mesh $2\times2\times2$. For calculations of positron parameters the supercells from VASP calculations were surrounded by additional cells with electron density calculated by atomic superposition to obtain $4\times4\times4$ supercells. The estimated relative uncertainty of the calculated positron parameters is about 10%.

Bulk positron lifetime τ_B and lifetime of positrons trapped in vacancy τ_V calculated using the four various approaches described above are collected in Table I and compared to positron lifetimes calculated by Barbiellini *et al.*[26] using GGA scheme with self-consistent electron density obtained by linear muffin-tin orbital (LMTO) method within the

atomic-spheres approximation (ASA). Similar results were recently obtained by Robles *et al.*[29] also using LMTO method with GGA scheme. Experimental positron lifetimes are listed in the last column of Table I. One can see that VASP-GGA and ATSUP-LDA approaches give similar results which are in the best agreement with experiment and also with the LMTO(ASA)-GGA calculations. Self-consistent electron density with LDA approach results in too short lifetimes because LDA overestimates positron-annihilation rate especially with *d* electrons.[26] This shortcoming is to some extent compensated by the use of Boroński-Nieminen enhancement with superimposed atomic electron density and neglecting the charge transfer.[19,30] For this reason, the ATSUP-LDA lifetimes are comparable to those obtained by the more precise VASP-GGA approach. On the other hand, the GGA scheme is more sensitive to details of electronic structure than LDA (Ref. 26) and should be, therefore, used with self-consistent electron density. Table I shows that lifetimes calculated using the ATSUP-GGA approach are too long compared to experiment.

Note that rigid Nb lattice was assumed in the calculations presented in Table I, i.e., relaxations of Nb atoms around vacancy were neglected in the present approach. In order to evaluate the magnitude of relaxations of Nb atoms around vacancy we performed ion relaxations by VASP and calculated relaxed geometry of Nb vacancy. It was found that nearest-neighbor Nb atoms relax toward vacancy. Their displacement with respect to the positions in the rigid lattice amounts to 0.08 Å, i.e., relative displacement is 2.4% of the lattice parameter. The lifetime of a trapped positron in vacancy with relaxed ions is about 15 ps shorter. However, it has to be mentioned that a localized positron *itself* influences positions of Nb ions surrounding a vacancy. Positron-induced forces can be calculated by Hellman-Feynman theorem and cause usually an outward relaxation of the neighboring ions.[31] Thus, to calculate realistic positron lifetime for relaxed defects it is necessary not only (i) to determine relaxed defect geometry without positron, but also (ii) to consider relaxations caused by positron-induced forces. Such demanding calculations are out of the scope of this work but represent a challenge for future theoretical approach. Recently Makkonen *et al.*[31] calculated positron-induced forces for vacancy in Si, Al, and Cu using the ATSUP-based approach. The obtained results showed that outward relaxation of the nearest-neighbor ions caused by positron trapped in vacancy is even larger than the inward ion relaxation around vacancy without positron. Hence, the outward relaxation caused by positron-induced forces and ion relaxation toward vacancy cancel at least partially each other and the assumption of rigid Nb lattice used in this work is reasonable. This is testified by the fact the positron lifetime for Nb vacancy calculated using VASP-GGA (i.e., the most precise approach) is in good agreement with experiment.

Self-consistent calculation of the momentum distribution of annihilating electron-positron pairs requires all-electron wave function and, therefore, is not straightforward even if the band structure was solved by VASP. Recently Makkonen *et al.*[31] developed a scheme for calculation of the momentum distribution of annihilating electron-positron pairs using the projector-augmented wave (PAW) method.[32] The all-electron wave function was constructed from the soft pseudovalence wave functions calculated by VASP applying a suitable transformation. The core states were treated within the frozen-core approximation, i.e., were approximated by free-atom wave functions.[31] Such calculations are, however, out of the scope of this paper. Here we restrict ourselves to ATSUP-based non-self-consistent approach[33,34] to calculate high-momentum part (HMP) of the momentum distribution of electrons which annihilated positrons. An electron state *j* described by the wave function ψ_j^- contributes to the momentum distribution of the annihilation photons by a component

$$M_j(\mathbf{p}) = \pi r_e^2 c \gamma_j \left| \int d\mathbf{r} \psi_j^-(\mathbf{r}) \psi^+(\mathbf{r}) \exp(-i\mathbf{pr}) \right|^2. \quad (4)$$

The symbol γ_j stands for the enhancement factor of the state *j*. The HMP of the momentum distribution comes almost exclusively from the localized core electrons. Equation (4) can be simplified considerably when only annihilations with core electrons are considered. The contribution of the *i*th atom and a shell characterized by quantum numbers *n* and *l* is given by the following formula:[33]

$$M_{i,nl}(p) = 4\pi^2 r_e^2 c N_{i,nl} \gamma_{i,nl} \left| \int dr R_i^+(r) R_{i,nl}^-(r) j_l(pr) r^2 \right|^2. \quad (5)$$

In this equation $N_{i,nl}$ denotes the number of electrons in the (n,l) shell, j_l is the spherical Bessel function, and $R_{i,nl}^-$ is electron radial-wave function. For the positron wave function we assume an isotropic form around each nuclei. The radial part R_i^+ of positron wave function around the *i*th nuclei is obtained by spherical averaging of the positron wave function ψ^+ in a sphere of radius r_a around the nuclei. The radius r_a was used also as an upper limit of the integral in Eq. (5). For Nb it was found that $r_a = 6$ a.u. is already enough to get results which do not change when this parameter is increased. The enhancement factor for the (n,l) shell of the *i*th atom is

$$\gamma_{i,nl} = \lambda_{i,nl}^{\mathrm{LDA,GGA}} / \lambda_{i,nl}^{\mathrm{IPM}}, \quad (6)$$

where the partial annihilation rates $\lambda_{i,nl}$ corresponding to the (n,l) core orbital of the *i*th atom are calculated from the equation

$$\lambda_{i,nl} = \pi r_e^2 c \int d\mathbf{r} |\psi^+(\mathbf{r})|^2 n_{i,nl}(|\mathbf{r} - \mathbf{r}_i|) \gamma[n(\mathbf{r})]. \quad (7)$$

In this equation $n_{i,nl}$ denotes the radial core electron density of the (n,l) orbital of the *i*th atom placed at position $\mathbf{r}_i$. The annihilation rates $\lambda_{i,nl}^{\mathrm{LDA,GGA}}$ were calculated using the LDA or GGA approach. The symbol $\lambda_{i,nl}^{\mathrm{IPM}}$ denotes the annihilation rates calculated within the independent-particle model (IPM), i.e., with $\gamma = 1$. The final one-dimension HMP which can be compared to the experimental CDB spectrum is obtained by summing up the contributions of the core states (n,l) of all atoms *i* in the system and integrating over the high-momentum tail

$$M(p) = \sum_{i,nl} \int_p^\infty dppM_{i,nl}(p). \quad (8)$$

In order to compare the calculated HMP curves to experimental CDB spectra, they have to be properly normalized. The areas of the experimental CDB spectra were scaled to unity, while the areas below the theoretical HMP curves were set equal to $\lambda_{\text{core}}/\lambda$, where

$$\lambda_{\text{core}} = \sum_{i,nl}^{\text{core}} \lambda_{i,nl} \quad (9)$$

is the annihilation rate with all core electrons of the system, while λ is the total annihilation rate given by Eq. (3). In order to mimic the effect of the finite resolution of the experimental setup, the theoretical HMP curves were convoluted with a Gaussian with FWHM of $4.0\times10^{-3}m_0c$. The following core electron configurations were considered: for Nb, the [Kr] core was taken and for H, $1s^1$ configuration was used.

B. Theoretical modeling of vacancy-hydrogen complexes

It is well known that hydrogen in a perfect Nb lattice occupies tetrahedral interstitial positions.[35] Vacancy represents a potential well for hydrogen and trapping of hydrogen in a vacancy was observed.[6,36,37] Thus, the hydrogen lowest energy sites are changed in Nb crystal containing vacancy. In order to model vacancy-hydrogen complexes it is necessary to determine the position of hydrogen trapped in a vacancy.

A simple approach to determine the equilibrium (i.e., the lowest energy) position of hydrogen trapped in a vacancy is the use of the effective-medium theory (EMT) formulated by Nørskov[38] and Stott and Zaremba.[39] It was shown that EMT describes correctly all the trends of hydrogen heats of solution in 3*d*, 4*d*, and 5*d* transition metals.[38] Calculations performed on Ni (Ref. 40) showed that EMT reproduces well the bond lengths, chemisorption energies, and vibrational frequencies of hydrogen. Moreover, it was shown[41] that hydrogen binding energies to interstitials, vacancies, and voids calculated by EMT for Cu, Ni, Pd, and Fe are in very good agreement with experimental data.[6,42,43] Finally, EMT calculations performed in Ref. 41 revealed that hydrogen trapped in a vacancy in Fe is located on the line connecting a vacancy and the nearest-neighbor octahedral interstitial position at the distance of $0.33a=0.94$ Å from a vacancy. This position, determined by EMT, is in excellent agreement with the hydrogen position determined in ion channeling experiment.[44] This success justifies the use of EMT also for determination of positions of hydrogen trapped in the Nb vacancy.

In this work we used the EMT approach described in details in Ref. 9. In case of vacancy surrounded by multiple hydrogen atoms the calculations in Ref. 9 were refined by including mutual interactions of hydrogen atoms surrounding a vacancy. In order to estimate reliability of the equilibrium hydrogen positions calculated by EMT, we determined the equilibrium position of hydrogen trapped in Nb vacancy also by self-consistent band-structure calculations using VASP code. Hydrogen atom is (i) substantially lighter than Nb atom and (ii) highly mobile even below room temperature.[2] Thus, in the VASP calculations, Nb atoms were fixed at the rigid-lattice positron and only H atoms were allowed to relax. Fully relaxed calculations of vacancy-hydrogen complexes should be a next step in the theoretical modeling, which is in the scope of the present paper.

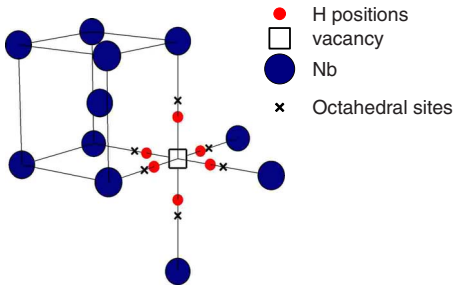

FIG. 1. (Color online) Schematic drawing of six crystallographically equivalent equilibrium positions of hydrogen trapped in vacancy calculated by EMT. Distance of hydrogen from the vacancy is $d_{v\text{-H}}=0.37a=1.22$ Å.

Both in EMT and VASP calculations, we assumed that symmetry of vacancy-hydrogen complexes is retained and configurations with the highest symmetry were considered. Thus, hydrogen-hydrogen (H-H) interaction may cause a change of distance $d_{v\text{-H}}$ of H atoms from the center of a vacancy, but all H atoms surrounding a vacancy are affected in the same way. In other words, H atoms surrounding a vacancy are indistinguishable and have the same distance $d_{v\text{-H}}$ from a vacancy center. However the distance $d_{v\text{-H}}$ depends on number of H atoms surrounding a vacancy.

The equilibrium (lowest energy) position of single H atom trapped in a vacancy was calculated by EMT in Ref. 9. It was found that hydrogen is located on the line between a vacancy and the nearest-neighbor octahedral interstitial site at the distance $d_{v\text{-H}}=0.37a=1.22$ Å from a vacancy. There are six such sites around a vacancy all crystallographically equivalent and they are shown schematically in Fig. 1.

Results of VASP calculations for a vacancy-hydrogen (v-H) complex are presented in Fig. 2 which shows the dependence of the total supercell energy on the hydrogen distance from vacancy $d_{v\text{-H}}$ in the [100] direction, i.e., on the line between a vacancy and the nearest-neighbor octahedral site. The minimum-energy site was found at the distance $d_{v\text{-H}}=0.41a=1.37$ Å, which is close to the lowest energy site calculated by EMT. The relative difference between the distance of the H atom from a vacancy determined by EMT and VASP is $\approx$10%. Taking into account that the EMT and VASP approach are based on completely different approximations, this can be considered as very reasonable agreement. The vacancy-hydrogen distance $d_{v\text{-H}}$ calculated using VASP and EMT, respectively, is plotted in Fig. 3 as a function of the number of H atoms surrounding a vacancy. The distances calculated by VASP are systematically higher than those obtained from EMT. Nevertheless the relative difference of the results calculated by VASP and EMT does not exceed 10% except of v-3H complex where it approaches 15%. Relative change $\Delta d_{v\text{-H}}/d_{v\text{-H}}$ of hydrogen distance calculated using VASP and EMT is shown in Fig. 4 as a function of number of

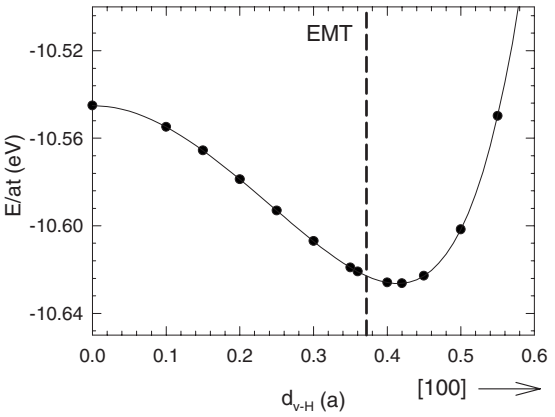

FIG. 2. Dependence of total supercell energy calculated by VASP on hydrogen distance from the vacancy in the [100] direction. The vacancy is located at the origin of coordinate system. The equilibrium vacancy-hydrogen distance calculated by EMT is plotted in the figure by a dashed line for comparison.

hydrogen atoms surrounding a vacancy. In both approaches we obtained similar trend: addition of second H atom to v-H complex causes shortening of $d_{v\text{-}H}$, i.e., H atoms relax *toward* a vacancy. On the other hand, for more than three H

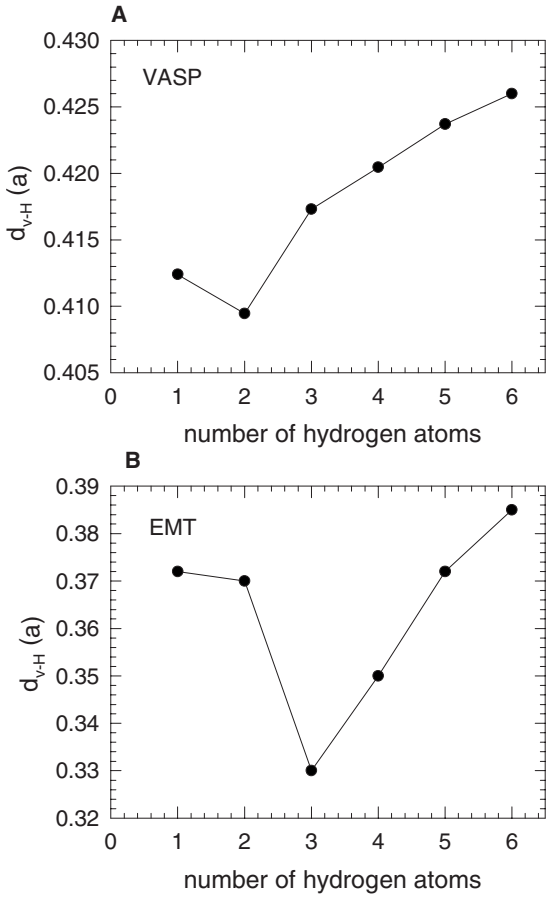

FIG. 3. Distance of hydrogen from vacancy $d_{v\text{-}H}$ as a function of number of H atoms surrounding the vacancy. (a) Results of VASP calculation and (b) EMT calculations. Distances are given in units of the Nb lattice parameter a.

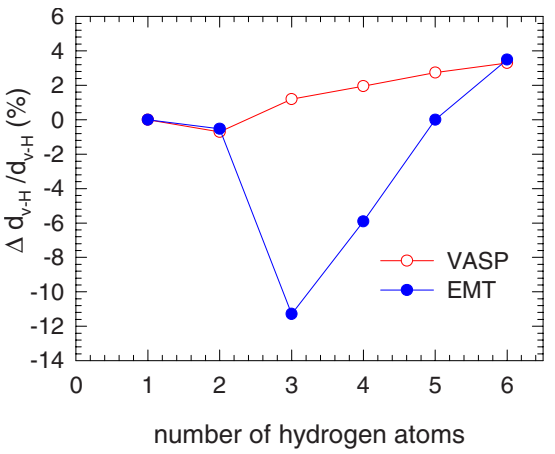

FIG. 4. (Color online) Relative change of hydrogen distance from the vacancy as a function of number of hydrogen atoms surrounding the vacancy; open symbols: VASP calculations, full symbols: EMT approach.

atoms, the H-H interaction becomes repulsive and H atoms relax outward from a vacancy.

Lifetimes of positrons trapped in vacancy-hydrogen complexes and corresponding positron binding energies are shown in Figs. 5 and 6, respectively, as a function of the number of hydrogen atoms surrounding a vacancy. Positron lifetimes and binding energies plotted in Figs. 5 and 6 were calculated using the four different approaches described in the Sec. III. In all cases positron lifetime and binding energy decrease monotonically with increasing number H atoms around a vacancy. Figure 5 shows that VASP-GGA and ATSUP-LDA approaches give relatively similar lifetimes. The largest difference between these two approaches was observed for nondecorated Nb vacancy. Positron lifetimes calculated by ATSUP-GGA scheme are slightly longer for v-5H and v-6H complexes. On the other hand, the VASP-LDA approach results in significantly shorter lifetimes, which testifies that LDA overestimates the positron-annihilation rate

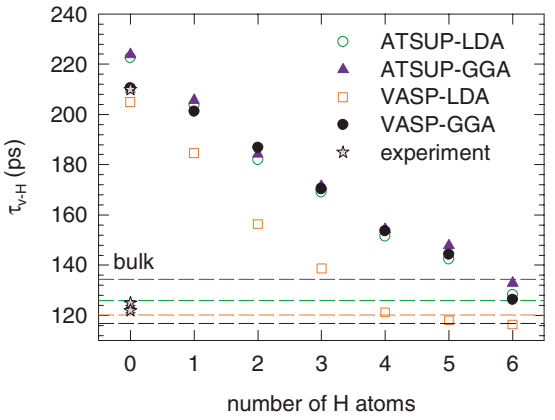

FIG. 5. (Color online) Dependence of lifetime $\tau_{v\text{-}H}$ of positron trapped at vacancy-hydrogen complex on the number of hydrogen atoms surrounding the vacancy. Dashed lines show the bulk positron lifetime calculated using the various approaches described in the text. Stars show the experimental lifetimes measured in Ref. 8 and in this work.

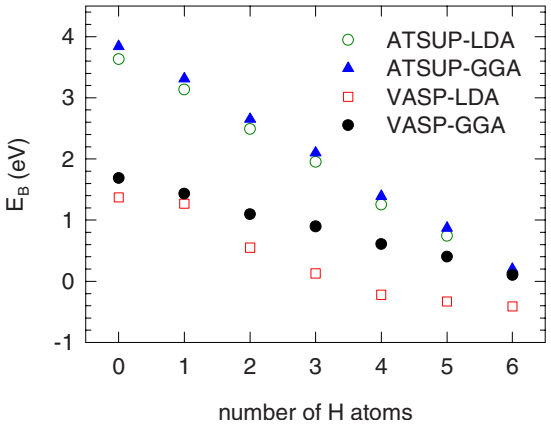

FIG. 6. (Color online) Dependence of the positron binding energy to vacancy-hydrogen complexes on the number of hydrogen atoms surrounding the vacancy. The binding energies were calculated using the four different schemes described in the text.

with the hydrogen electron. This shortcoming of LDA is to some extent compensated in the ATSUP-LDA approach when atomic orbitals are used and the hydrogen electron is kept localized in $1s$ orbital, which results in a reduction of positron-annihilation rate with the hydrogen electron. The positron lifetime for a vacancy surrounded by six hydrogen (v-6H complex) approaches the bulk positron lifetime and the corresponding binding energy decreases basically down to zero. Hence, the v-6H complex is likely unable to confine the positron anymore. The bulk lifetime "level" differs in the various computational schemes (see Fig. 5), therefore, we plotted in Fig. 7 the ratio $\tau_{v\text{-H}}/\tau_B$. One can see in this figure again that $\tau_{v\text{-H}}/\tau_B$ ratios calculated by VASP-GGA and ATSUP-LDA are relatively similar, while ATSUP-GGA and VASP-LDA give too low values of $\tau_{v\text{-H}}/\tau_B$. Figure 6 demonstrates that positron binding energy to vacancy-hydrogen complexes is more sensitive to details of electronic structure than positron lifetime. Use of self-consistent electron density results in significantly lower positron binding energy. Thus, VASP-GGA approach is necessary for a precise determination of

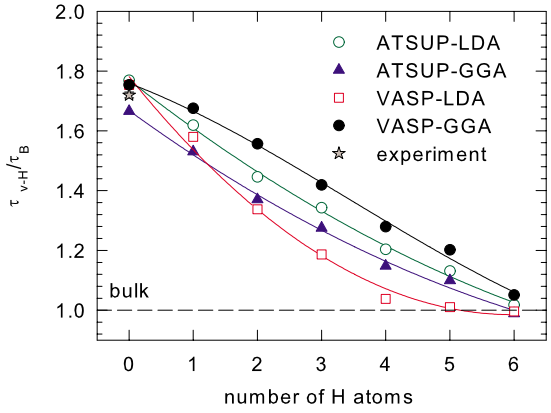

FIG. 7. (Color online) Dependence of ratios $\tau_{v\text{-H}}/\tau_B$ calculated using the four various schemes described in the text on the number of hydrogen atoms surrounding the vacancy. Solid lines are polynomial fits to guide eyes only. Dashed line corresponds to the bulk positron lifetime.

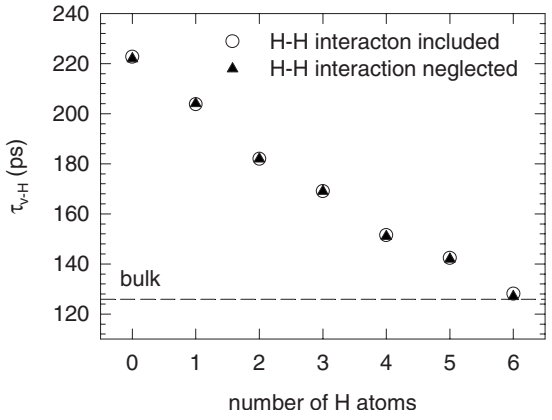

FIG. 8. Lifetimes of positrons trapped at vacancy-hydrogen complexes calculated using ATSUP-LDA approach with H-H interaction included (open circles, this work) and using a simplified ATSUP-LDA approach with neglected H-H interaction (full triangles, Ref. 9). Dashed line corresponds to the bulk positron lifetime.

positron binding energy to vacancy-hydrogen complexes.

Influence of H-H interactions on the positron lifetime is illustrated in Fig. 8 which compares lifetimes of positrons trapped in vacancy-hydrogen complexes calculated using (i) the ATSUP-LDA scheme used in this work with H-H interaction included and (ii) a simplified ATSUP-LDA approach used in Ref. 9, where H-H interaction was neglected. In the latter case no relaxations of H atoms were performed and vacancies surrounded by multiple H atoms were modeled simply by filling the appropriate number of the lowest energy sites around a vacancy calculated by EMT (see Fig. 1) with H atoms. Figure 8 demonstrates that H-H interaction has only a very small effect on the lifetime of positrons trapped at a vacancy. Similar conclusion was obtained also for positron binding energy.

IV. EXPERIMENTAL RESULTS AND DISCUSSION

A. Nonirradiated specimens

Results of LT measurements are summarized in Table II. The annealed Nb specimen exhibits a single-component LT spectrum with a lifetime $\tau_B = 128$ ps, which agrees with the calculated bulk Nb lifetime of 126 ps. Thus, the annealed Nb specimen can be considered as a "defect-free" material because virtually all positrons annihilate from the free state. No new defects detectable by LT spectroscopy were created by sputtering of the Pd (or Cr) cap onto the annealed specimen (see Table II).

The $S(E)$ curve measured on the annealed specimen is plotted in Fig. 9. The positron diffusion length $L_{B,+} = (319 \pm 8)$ nm was obtained from fitting of the $S(E)$ curve by VEPFIT. The $S(E)$ curve measured on the annealed specimen after sputtering of the Cr cap is plotted in Fig. 9 as well. The curve was fitted by VEPFIT assuming now two layers: (i) Cr cap and (ii) Nb bulk. Note that the thickness of the Cr overlayer was fixed at the value of 30 nm known from sputtering. A positron diffusion length of (300 ± 10) nm was obtained now from fitting for bulk Nb. This value is compa-

TABLE II. Summary of results of LT measurements. The nonirradiated specimens generally exhibit a single-component spectrum, whereas LT spectra of the irradiated specimens could be decomposed into two components. The symbol τ_f denotes the quantity calculated from Eq. (11) in order to check the consistency of the decomposition with the two-state simple trapping model.

Specimen	τ_{I} (ps)	I_{I} (%)	τ_{II} (ps)	I_{II} (%)	τ_f (ps)
		Nonirradiated			
Annealed	128.3(4)	100			
Cr cap deposited	127.6(6)	100			
Pd cap deposited	128.0(5)	100			
		Irradiated			
Bare specimen	48(6)	16(1)	190.7(5)	85(1)	131(1)
With Cr cap	54(5)	14.2(7)	183.5(5)	85.8(7)	137(1)
With Pd cap	57(7)	17.0(8)	185.8(8)	83.0(8)	140(1)
Pd cap deposited after irradiation	47(9)	15(2)	190.0(8)	85(2)	131(1)
		H loaded			
With Pd cap	60(9)	11(2)	149(3)	89(2)	128(1)

rable to that for the annealed specimen prior to the Cr cap sputtering, thus testifying that sputtering of the Cr cap did not cause any sensible damage in Nb. The positron diffusion length in the Cr cap was found to be (30 ± 10) nm only. Such a low positron diffusion length gives evidence that the sputtered Cr overlayer is far from being a perfect material and contains a high density of open-volume defects. A similar result was obtained in case of the Pd overlayer.

B. Electron-irradiated specimens

The average path length [continuous slowing down approximation (CSDA) range], traveled by a 10 MeV electron in Nb until it slows down to rest, was estimated to be 7 mm by ESTAR (Ref. 45) in the continuous slowing down approximation. Thus, assuming an exponential electron implantation profile, the difference in the number of stopped electrons on the irradiated side and on the opposite side of a 0.5 mm thick Nb specimen is less than 7%. Figure 10 shows the $S(E)$ curves measured on both sides of the irradiated specimen (i.e., the irradiated side and the opposite side). The bulk S parameter measured on the irradiated side is only very slightly higher than that measured on the opposite side. This confirms the assessment mentioned above. Note that all the measurements which will be reported further in this paper were taken on the specimens' irradiated side.

The $S(E)$ curves for the virgin and irradiated specimens are compared in Fig. 11. It is clear that the bulk value of the S parameter is increased in the irradiated specimens due to irradiation-induced defects. The curves were fitted by VEPFIT,

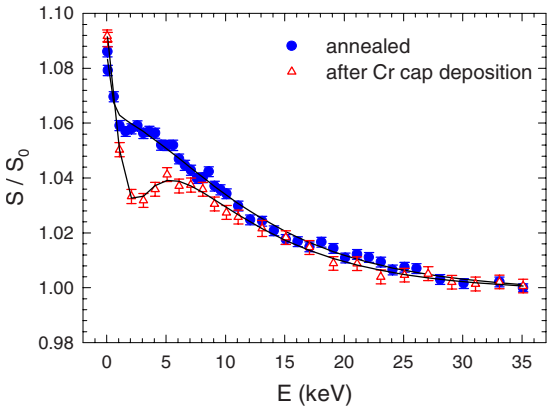

FIG. 9. (Color online) Dependence of the S parameter on the positron energy E for nonirradiated Nb specimens: full circles—annealed specimen, open triangles—the annealed specimen covered with a Cr overlayer. Solid lines show the model functions fitted by VEPFIT.

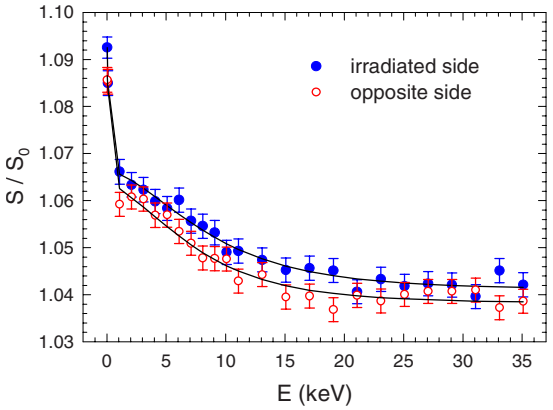

FIG. 10. (Color online) The $S(E)$ curves measured on bare Nb irradiated with electrons: full circles—the irradiated side, open circles—the opposite side. Solid lines show the model functions fitted by VEPFIT.

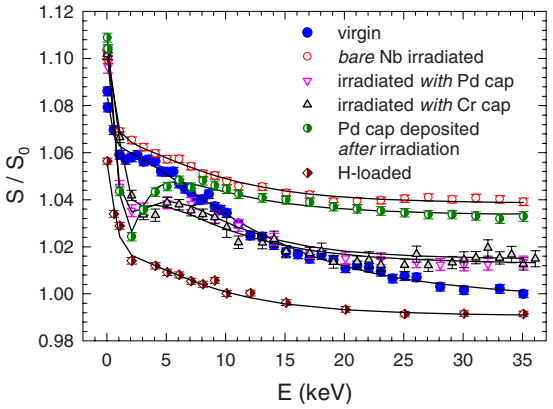

FIG. 11. (Color online) The $S(E)$ curves for virgin (nonirradiated) and electron-irradiated Nb specimens. Solid lines show the model functions fitted by VEPFIT.

assuming a single layer in case of *bare* Nb specimen, whereas two layers were considered in case of Nb covered with a Pd/Cr cap. The results of fitting are summarized in Table III. The following conclusions can be drawn from the SPIS results:

(i) The bulk value of the S parameter is increased in irradiated specimens and this increase is accompanied by a shortening of the positron diffusion length L_+. This behavior testifies that positrons in the irradiated specimens are trapped at defects created by electron irradiation.

(ii) The highest increase of S was observed in the bare Nb specimen irradiated with electrons.

(iii) Deposition of the Pd cap *after* irradiation leads to only a slight change of the S parameter value. On the other hand, the specimens irradiated with the Pd (or Cr) cap, i.e., the overlayer was deposited *prior* to irradiation, exhibit a significantly lower S parameter.

(iv) The Pd (or Cr) overlayer is characterized by a positron diffusion length in the range (15–40) nm in all irradiated specimens testifying, thus, that the overlayer retains in a highly defected structure detected already in the nonirradiated specimens.

TABLE III. Summary of results of SPIS and XRD measurements. The symbols L_+, $\Delta S/S_0$ denote the positron diffusion length and the relative change of the bulk S parameter for Nb specimens obtained from fitting of the experimental $S(E)$ curves by VEPFIT. The lattice constant a determined by XRD is shown in the last column. The abbreviation n.a. means not analyzed.

Specimen	L_+ (nm)	$\Delta S/S_0$ (%)	a (Å)
	Nonirradiated		
Annealed	319(8)	0.0	3.3033(3)
Cr cap deposited	300(10)	0.2(2)	n.a.
Pd cap deposited	300(10)	0.3(2)	n.a.
	Irradiated		
Bare specimen	178(6)	5.1(2)	3.3043(3)
With Cr cap	200(10)	2.3(2)	3.3024(4)
With Pd cap	190(10)	2.6(2)	3.3016(2)
Pd cap deposited after irradiation	175(7)	4.5(3)	3.3020(3)
	H loaded		
With Pd cap	200(10)	−0.27(1)	3.3090(5)

The lattice parameters a measured by XRD are listed in the last column in Table III. The a values measured on the annealed (nonirradiated) Nb specimen agree well with the value reported in the PDF-2 database.[46] No increase of a could be detected in irradiated specimens (except the specimen loaded with hydrogen, which will be discussed in Sec. IV C). The highest a value was measured on the bare Nb specimen irradiated with electrons. The relative lattice expansion in the α phase range of hydrogen concentrations is directly proportional to the hydrogen concentration in the sample

$$\frac{a-a_0}{a_0} = \xi c_{\mathrm{H}}. \tag{10}$$

The symbol a states for the lattice constant of a sample with hydrogen concentration c_H, while a_0 denotes now the lattice constant of a hydrogen-free virgin sample. The coefficient ξ=0.058 can be found in the literature for bulk Nb.[35] Using Eq. (10), it can be concluded that the hydrogen concentration in the bare Nb irradiated with electrons is lower than ~5000 ppm. Note that $c_{\mathrm{H}} \sim 2000$ ppm was estimated as a sensitivity limit of the XRD setup used in this work.

LT spectra of the irradiated Nb specimens can be fitted by two components (see Table II). The first component with lifetime $\tau_I < \tau_B$, which is a fitting parameter representing a combination of the bulk positron lifetime and positron trapping rates,[47] comes apparently from free positrons. The longer component with lifetime τ_{II} can be attributed to positrons trapped at defects. The latter component cannot be explained by positron trapping at irradiation-induced nondecorated Nb vacancies because τ_{II} is remarkably shorter than the calculated Nb-vacancy lifetime (see Table I). As was already explained in Sec. I, a shortening of the positron lifetime is caused by H atoms attached to vacancies. In order to clearly identify these vacancy-hydrogen complexes, the number of attached H atoms has to be determined. Figure 12 shows lifetimes of trapped positrons calculated by VASP-GGA and ATSUP-LDA approach as a function of the number of H atoms surrounding a vacancy. The positron lifetime monotonically decreases with increasing number of H atoms, from $\tau_v \approx 210-223$ ps for a nondecorated Nb vacancy down to a value which approaches the bulk Nb lifetime τ_B. The lifetimes τ_{II} measured on the irradiated specimens fall between the lifetime $\tau_{v\text{-H}}$=204 ps for a v-H complex and $\tau_{v\text{-2H}}$=182 ps for a v-2H complex. This suggests that the irradiated specimens contain a mixture of v-H and v-2H complexes. Positrons trapped at both types of complexes contribute to the component with lifetime τ_{II} in LT spectrum.

The quantity τ_f is often used to test the consistency of a LT spectrum decomposition with the simple trapping model (STM).[48] It can be calculated from the expression

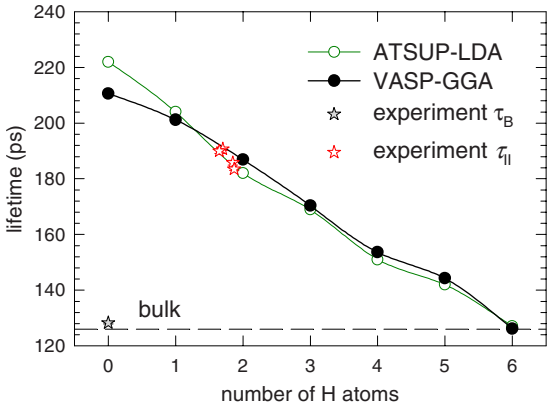

FIG. 12. (Color online) Calculated lifetime of positron trapped in a Nb vacancy surrounded by a varying number of H atoms: full circles—VASP-GGA, open circles—ATSUP-LDA. Experimental lifetime τ_{II} of positrons trapped at defects in irradiated specimens are plotted by open stars. The mean number of H atoms surrounding vacancies in irradiated specimens was calculated as $(c_{v\text{-H}}+2c_{v\text{-2H}})/(c_{v\text{-H}}+c_{v\text{-2H}})$ (see Sec. IV E). The experimental bulk positron lifetime is shown by the filled gray star.

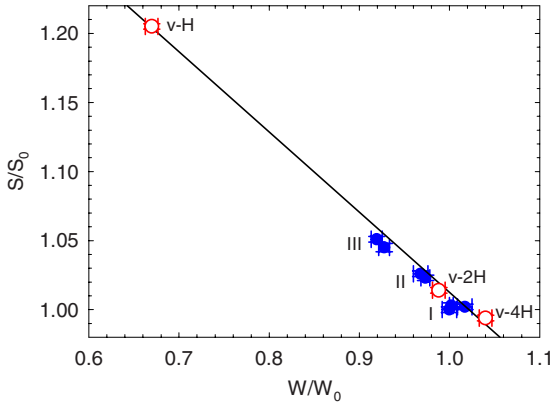

FIG. 13. (Color online) *S*-*W* plot for the specimens studied; the bulk *S* and *W* parameters measured by SPIS fall into three well-separated groups: I—nonirradiated specimens, II—specimens irradiated *with* Pd (or Cr) cap, and III—specimens irradiated *without* any cap. The *S* and *W* parameters calculated for *v*-H, *v*-2H, and *v*-4H complexes using Eqs. (21)–(23), (26), and (27) are plotted by open symbols and are connected by a solid line.

$$\tau_f = \left(\sum_i \frac{I_i}{\tau_i} \right)^{-1}, \tag{11}$$

where τ_i and I_i are lifetimes and relative intensities of the exponential components resolved in a LT spectrum. If the STM is applicable (i.e., the STM assumptions are fulfilled), then

$$\tau_f = \tau_B. \tag{12}$$

The quantity τ_f calculated for the two-component decomposition of LT spectra of irradiated specimens is shown in the last column of Table II. Clearly, the obtained τ_f values are slightly higher than τ_B indicating that the two-state STM cannot be applied because the specimens contain more than just a single type of defect.

In order to separate the contribution of *v*-H and *v*-2H complexes, the LT spectra were then decomposed into three components with fixed lifetimes $\tau_{v\text{-H}}$ and $\tau_{v\text{-2H}}$, while the lifetime τ_1 of the shortest component, which represents a contribution of free positrons, was fitted as a free parameter. The results of this decomposition are shown in Table IV together with the quantity τ_f calculated for the three-component decomposition using Eq. (11). It is obvious that in case of the three-component decomposition, τ_f agrees very well with τ_B testifying that the assumptions of the three-state STM are fulfilled.

From the three-component decomposition it becomes clear that *v*-2H complexes represent the dominant type of defects in all irradiated specimens. The LT results confirmed the conclusion obtained from SPIS studies that the deposition of a Pd cap *after* irradiation has a negligible effect on defects in the specimen. On the other hand, the specimens irradiated *with* Pd (or Cr) cap exhibit a higher relative fraction of *v*-2H complexes. Hence, the irradiation-induced vacancies in the specimens irradiated with a Pd (or Cr) cap are *on average* surrounded by more H atoms. This is well visible also on the *S*-*W* plot in Fig. 13, created from bulk *S* and *W* parameters for Nb specimens measured by SPIS. One can see that all points fall with a reasonable precision on a straight line, indicating that *S* and *W* change approximately linearly with increasing hydrogen content in the vicinity of a vacancy. Three well-separated groups appeared in the *S*-*W* plot:

TABLE IV. Results of three-component decomposition of LT spectra of electron-irradiated Nb specimens. The lifetimes $\tau_2=\tau_{v\text{-2H}}=182$ ps (*v*-2H) and $\tau_3=\tau_{v\text{-H}}=204$ (*v*-H) were fixed. The last column shows the quantity τ_f calculated from Eq. (11) which was used to test consistency of the decomposition with the three-state STM.

Specimen	τ_1 (ps)	I_1 (%)	I_2 (%)	I_3 (%)	τ_f (ps)
		Irradiated			
Bare specimen	43(8)	14(2)	61(2)	25(3)	128(1)
With Cr cap	48(5)	15(2)	74(1)	11(9)	129(1)
With Pd cap	52(7)	17(1)	71(2)	12(3)	129(1)
Pd cap deposited after irradiation	44(9)	14(2)	57(2)	29(4)	129(1)

(i) defect-free nonirradiated specimens, (ii) specimens irradiated *with* Pd (or Cr) cap, and (iii) specimens irradiated *without* any cap. The irradiation-induced vacancies are in case (ii) surrounded *on average* by more H atoms than in case (iii). It is seen in lower S and higher W parameter which shifted the case (ii) toward the nonirradiated specimens.

Thus, we can conclude that there is an irradiation-assisted pickup of hydrogen into Nb specimens, which is in concordance with the picture suggested in Refs. 8 and 49. Electron irradiation may contribute to hydrogen uptake in two ways: (i) energetic electrons ionize water vapor and H_2 molecules present in the air, and moreover (ii) electron bombardment may break at least locally the thin oxide layer grown on Nb (and also Cr) surface which under normal conditions represents a barrier for hydrogen penetration into the specimens.

C. Hydrogen-loaded specimens

The specimen irradiated with Pd cap and subsequently loaded with hydrogen exhibits remarkably higher lattice parameter compared to the other samples. From Eq. (10) one can estimate that hydrogen concentration in this specimen is $c_H=0.03$ atom^{-1}. This value agrees well with the amount of hydrogen introduced into the specimen calculated from the Faraday's law.

LT spectrum of the hydrogen-loaded specimen can be well fitted by two components, which are shown in Table II. Similarly to the irradiated specimens, the shorter component with lifetime τ_I comes from free positrons, while the longer component with lifetime τ_{II} can be attributed to positrons trapped at defects. The lifetime τ_{II} is very close to that calculated for v-4H complexes. Indeed, v-4H complexes were found to be created by H loading in well-annealed Nb specimens.[9] Hence, the LT results indicate that v-4H complexes were created also in the irradiated specimen doped subsequently with hydrogen. Majority of H atoms introduced by electrochemical charging occupy the tetrahedral interstitial positions and cause a remarkable lattice expansion detected by XRD (see Table III). However, some of them become trapped at the irradiation-induced vacancies surrounded already by one or two H atoms. Thus, the number of H atoms surrounding vacancies increases until all the irradiation-induced vacancies become surrounded by 4 H atoms. It was found in Ref. 9 that Nb vacancies surrounded by more than 4 H atoms become unstable, i.e., v-4H complex represents a stable configuration with maximum number of H atoms. Note that H atoms introduced by charging are able to find available trapping sites easily because of their high mobility. In addition to H trapping at v-H and v-2H complexes existing already in the irradiated specimens, additional vacancies (again surrounded by hydrogen) can be introduced by hydrogen loading as was found in Ref. 9. Thus, contrary to the as-irradiated specimen, the specimen loaded with hydrogen contains v-4H complexes as a *single* type of defects. This is supported also by the fact that τ_f values calculated from Eq. (11) agree well with the bulk lifetime τ_B (see Table II).

D. HPT-deformed specimens

It is generally accepted that the dislocation line is only a shallow positron trap but represents a channel for rapid diffusion of positron.[50] Once a positron is trapped at dislocation, it diffuses quickly along the dislocation line and becomes finally trapped at a vacancy anchored in the elastic field of the dislocation.[50] Thus, the final positron trap in plastically deformed material is a vacancylike defect with open volume slightly reduced due to the compressive stress field of dislocation.

Nb specimen deformed by HPT exhibits a two-component LT spectrum. Both the components resolved in the LT spectrum exhibit positron lifetimes significantly longer than τ_B and can be, therefore, attributed to positrons trapped at defects. Hence, virtually all positrons in HPT-deformed specimen annihilate from a trapped state at defects (saturated trapping) testifying a high defect density in HPT-deformed specimen. The dominating component with relative intensity of $(93.6\pm0.8)\%$ and lifetime of (173.6 ± 0.3) ps comes from positrons trapped at dislocations, i.e., at vacancies anchored in the compressive stress field of the dislocation line. A high dislocation density ($\sim10^{14}$ m^{-2}) in the HPT-deformed specimen was confirmed by transmission electron microscopy. The remaining weak component with intensity of $(6.4\pm0.8)\%$ and lifetime of (300 ± 10) ps represents a contribution of positrons trapped at small vacancy clusters formed during the severe plastic deformation.[51]

E. Concentration of irradiation-induced defects

1. Concentration of defects in irradiated specimens

The concentrations $c_{v\text{-H}}$ and $c_{v\text{-2H}}$ of v-H and v-2H complexes can be calculated from LT results collected in Table IV using the three-state STM (Ref. 48)

$$c_{v\text{-H}}=\frac{I_2}{\nu_{v\text{-H}}}\frac{\tau_2-\tau_1}{\tau_1\tau_2}, \tag{13}$$

$$c_{v\text{-2H}}=\frac{I_3}{\nu_{v\text{-2H}}}\frac{\tau_3-\tau_1}{\tau_1\tau_3}, \tag{14}$$

where $\nu_{v\text{-H}}$ and $\nu_{v\text{-2H}}$ denote the specific trapping rate for v-H and v-2H complexes, respectively. Determination of the specific trapping rate is not straightforward because it requires one to determine the *absolute* concentration of defects independently, e.g., by another experimental technique. The specific positron trapping rate $(1.1\pm0.2)\times10^{15}$ s^{-1} was reported for a nondecorated vacancy in iron.[52] By multiplying this value by the ratio of the atomic density of Fe and Nb, we obtain an estimation of the specific trapping rate for a nondecorated Nb vacancy $\nu_v\approx1.0\times10^{15}$ s^{-1}. Vacancy-hydrogen complexes are less efficient positron traps, i.e., the corresponding specific trapping is lower compared to a nondecorated vacancy. It was shown[53] that the specific trapping rate for small (i.e., vacancylike) defects is proportional to (i) the positron binding energy E_B to the defect and also to (ii) the open volume of the defect. Hence, the specific trapping rate $\nu_{v\text{-}n\text{H}}$ for a vacancy surrounded by n H atoms can be estimated from the calculated positron binding energies plotted in Fig. 6

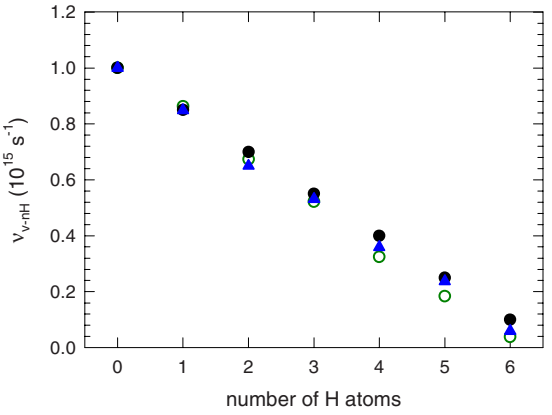

FIG. 14. (Color online) The specific positron trapping rate $\nu_{v\text{-}n\mathrm{H}}$ plotted as a function of the number of H atoms surrounding vacancy. The specific trapping rates were estimated from approximate open volume of v-nH complex using Eq. (16), full circles, and also from theoretically calculated positron binding energies using Eq. (15). Binding energies were calculated within ATSUP-LDA scheme (open circles) and VASP-GGA scheme (full triangles).

$$\nu_{v\text{-}n\mathrm{H}} \approx \nu_v \frac{E_B^{v\text{-}n\mathrm{H}}}{E_B^v}, \tag{15}$$

where E_B^v and $E_B^{v\text{-}n\mathrm{H}}$ denote the positron binding energy for a nondecorated vacancy and a v-nH complex, respectively. Alternatively, the specific trapping rate $\nu_{v\text{-}n\mathrm{H}}$ can be estimated also considering the open volume of v-nH complexes

$$\nu_{v\text{-}n\mathrm{H}} \approx \nu_v \frac{r_{v\text{-}n\mathrm{H}}^3}{r_v^3}, \tag{16}$$

where $r_v = 1.43$ Å is the diameter of Nb atom, i.e., half of the nearest-neighbor distance of Nb atoms. The open volume of a v-nH complex can be characterized by a sphere with radius $r_{v\text{-}n\mathrm{H}}^3$ given as

$$r_{v\text{-}n\mathrm{H}}^3 = \frac{1}{6}[n r_{\mathrm{H}}^3 + (6-n) r_v^3], \tag{17}$$

where $r_{\mathrm{H}} = 0.69$ Å is obtained by subtracting the "radius" of a H atom (Bohr radius 0.53 Å) from the distance 1.22 Å of the H atom from the center of a vacancy. Hence, if Nb and H atoms are represented by hard spheres with radius 1.43 and 0.53 Å, then $\frac{4}{3}\pi r_{v\text{-}n\mathrm{H}}^3$ is a weighted average of volumes of these spheres. The specific trapping rates estimated from Eqs. (15) and (16) are plotted in Fig. 14. Obviously, there is very reasonable agreement between the $\nu_{v\text{-}n\mathrm{H}}$ values obtained by the two different approaches. The specific trapping rate for v-2H complex is about 25% lower than that for v-H.

The concentrations of vacancy-hydrogen complexes estimated using Eqs. (13) and (14) are collected in Table V. The relative fraction of v-2H complexes in bare Nb irradiated with electrons is 75%. A similar value was found also in the specimen with a Pd cap deposited *after* irradiation. On the other hand, the relative fraction of v-2H complexes in specimens irradiated *with* a Pd (or Cr) cap is ≈90%. From the results in Table V it can be calculated that irradiation-induced vacancies in specimens irradiated *without* any cap are *on average* surrounded by ≈1.7 H atoms, while vacancies in those specimens irradiated *with* a Pd (or Cr) cap are *on average* surrounded by ≈1.9 H atoms.

TABLE V. Estimated concentrations of irradiation-induced defects and hydrogen in the irradiated specimens. $c_{v\text{-}\mathrm{H}}$ and $c_{v\text{-}2\mathrm{H}}$ denote concentration of v-H and v-2H complexes, respectively, calculated from LT results using Eqs. (13) and (14), c_D is the net concentration of irradiation-induced defects estimated from SPIS results using Eq. (19), c_H denotes the hydrogen concentration in the specimens estimated using Eq. (18).

Specimen	$c_{v\text{-}\mathrm{H}}$ (ppm)	$c_{v\text{-}2\mathrm{H}}$ (ppm)	c_D (ppm)	c_H (ppm)
	Irradiated			
Bare specimen	5.6(6)	17(2)	26(5)	41(1)
With Cr cap	2.2(5)	19(2)	19(5)	41(1)
With Pd cap	2.2(5)	16(3)	22(4)	36(2)
Pd cap deposited after irradiation	6.6(9)	17(2)	27(5)	40(2)

Hence, vacancies in the capped specimens are *on average* surrounded by more hydrogen atoms than those in the specimens irradiated without any cap. In case of Pd overlayer, this can be explained by the well-known catalytic effect in this overlayer, which enhances the hydrogen uptake into Nb.[54] A thin Pd layer with its lower desorption energy compared to Nb prevents the preferential occupation of subsurface sites over bulk sites, but keeps the surface relatively clean and with enough sites for dissociation of incoming hydrogen molecules.[54] Since Cr exhibits also a lower desorption energy than Nb,[55] a thin Cr overlayer is expected to enhance the hydrogen uptake in a similar manner as a Pd cap. The experimental lifetimes τ_{II} (Table II) were inserted into Fig. 12. The x coordinate of these points is the average number of H atoms surrounding a vacancy. Obviously, the experimental results are consistent with the theoretical prediction because all points fall quite well on the calculated dependence.

Taking into account a high mobility of hydrogen in Nb at room temperature,[2,3] it is reasonable to assume that all hydrogen present in the irradiated specimens are trapped at vacancies. The hydrogen concentration c_{H} in the specimens can be then estimated as

$$c_{\mathrm{H}} = c_{v\text{-}\mathrm{H}} + 2c_{v\text{-}2\mathrm{H}}. \tag{18}$$

The c_{H} values obtained from Eq. (18) for the irradiated specimens are shown in Table V. Apparently, all the irradiated specimens contain approximately the same amount of hydrogen. However, the estimated hydrogen concentration is below the sensitivity of XRD measurements. This explains why virtually no lattice expansion could be detected in the irradiated specimens by XRD (see Table III).

The net concentration of irradiation-induced defects c_D can be estimated also from SPIS results using equation

$$c_D = \frac{1}{\nu_D \tau_B}\left(\frac{L_{B,+}^2}{L_+^2} - 1\right), \tag{19}$$

where L_+ is the positron diffusion length measured on the irradiated specimen. The v-H and v-2H complexes cannot be

separated in the evaluation of SPIS data. The effective specific trapping rate ν_D is therefore

$$\nu_D = \frac{c_{v\text{-H}}\nu_{v\text{-H}} + c_{v\text{-2H}}\nu_{v\text{-2H}}}{c_{v\text{-H}} + c_{v\text{-2H}}}. \quad (20)$$

The net defect densities c_D calculated using Eq. (19) are collected in Table V. It can be concluded that the net concentration of irradiation-induced defects c_D estimated from SPIS data is in very reasonable agreement with $c_{v\text{-H}}+c_{v\text{-2H}}$ obtained from LT measurements. Since the specimens were irradiated up to a fluence $\Phi=10^{16}$ cm^{-2}, seven vacancies were *on average* created by a single electron.

The bulk S parameter for the irradiated specimens can be expressed as

$$S = S_0 f_0 + S_{v\text{-H}} f_{v\text{-H}} + S_{v\text{-2H}} f_{v\text{-2H}}, \quad (21)$$

where $S_0=1$ is the S parameter in defect-free Nb, $S_{v\text{-H}}$ and $S_{v\text{-2H}}$, respectively, are the S parameters corresponding to positrons trapped at v-H and v-2H complexes. The fraction of positrons annihilated in v-H and v-2H complexes, respectively, can be calculated from LT results (Table IV) using the three-state STM (Ref. 48)

$$f_{v\text{-H}} = \frac{I_2(\tau_2 - \tau_1)}{\tau_2} \quad (22)$$

and

$$f_{v\text{-2H}} = \frac{I_3(\tau_3 - \tau_1)}{\tau_3}. \quad (23)$$

An expression equivalent to Eq. (21) can be written also for the W parameter. Thus, using the LT results in Table IV and Eqs. (21)–(23), one can determine the S and W parameters of positrons trapped at v-H and v-2H complexes to be

$$S_{v\text{-H}} = 1.205(1), \quad W_{v\text{-H}} = 0.670(7),$$

$$S_{v\text{-2H}} = 1.014(1), \quad W_{v\text{-2H}} = 0.988(7),$$

which are shown in Fig. 13. Obviously all experimental points fall well on the line connecting the two calculated points corresponding to a pure contribution of v-H and v-2H complexes, respectively. This is an additional evidence that the irradiated specimens contain mixed v-H and v-2H complexes.

2. Concentration of defects in H-loaded specimen

The H-loaded specimen contains a single type of defect only, i.e., v-4H complexes. Concentration of v-4H complexes can be estimated from the LT results in Table II applying the two-state STM (Ref. 48)

$$c_{v\text{-4H}} = \frac{I_{\text{II}}}{\nu_{v\text{-4H}}} \frac{\tau_{\text{II}} - \tau_{\text{I}}}{\tau_{\text{I}}\tau_{\text{II}}}. \quad (24)$$

Independently it can be calculated also from SPIS results as

$$c_{v\text{-4H}} = \frac{1}{\nu_{v\text{-4H}}\tau_B}\left(\frac{L_{B,+}^2}{L_+^2} - 1\right), \quad (25)$$

where L_+ is the positron diffusion length measured on the H-loaded specimen. The concentrations of v-4H complexes given by Eqs. (24) and (25), respectively, are (25 ± 2) and (33 ± 5) ppm. Hence, the concentration of v-4H complexes in the H-loaded specimen is comparable to the net defect concentration in the irradiated specimens.

The bulk S parameter for the H-loaded specimen is a sum of a contribution of free positrons and positrons trapped at v-4H complexes

$$S = S_0(1 - f_{v\text{-4H}}) + S_{v\text{-4H}} f_{v\text{-4H}}, \quad (26)$$

where $S_0=1$ is the S parameter in defect-free Nb and $S_{v\text{-4H}}$ is the S parameter corresponding to positrons trapped at v-4H complexes. The fraction of positron annihilations at v-4H complexes, $f_{v\text{-4H}}$, can be calculated from the LT results in Table II using two-state STM (Ref. 48)

$$f_{v\text{-4H}} = \frac{I_{\text{II}}(\tau_{\text{II}} - \tau_{\text{I}})}{\tau_{\text{II}}}. \quad (27)$$

Equation (26) can be written also for the W parameter. Hence the S and W parameters corresponding to positrons trapped at v-4H complexes can be determined from Eqs. (26) and (27)

$$S_{v\text{-4H}} = 0.994(2), \quad W_{v\text{-4H}} = 1.040(7).$$

These values are included in the S-W plot in Fig. 13. It has to be mentioned that the point corresponding to v-4H complex falls well on the line connecting v-H and v-2H complexes. This clearly indicates that the increasing number of H atoms leads to a gradual increase of the W parameter due to increasing contribution of core electron annihilations and a decrease of the S parameter.

F. CDB studies

Hydrogen atoms surrounding irradiation-induced vacancies could be detected by CDB. To examine this possibility, we first performed a series of HMP calculations for a Nb vacancy surrounded by various numbers of H atoms located at the lowest energy positions determined by EMT (see Sec. III B). Figure 15 compares the experimental CDB profile measured on the nonirradiated annealed Nb specimen to HMP curves calculated using ATSUP-LDA and ATSUP-GGA approaches. In general, the HMP curves calculated using ATSUP-LDA approach are slightly higher than those calculated by ATSUP-GGA. This is due to the well-known fact that LDA approximation of electron-positron correlation overestimates annihilation with core electrons.[26]

The outer $4d$ and $5s$ Nb electrons are not localized in atomic orbitals but constitute metallic bonding in the crystal. Hence, these outer electrons should contribute to the main *low*-momentum part of the annihilation peak, while the dominant contribution into the *high*-momentum part of the annihilation peak comes from core electron orbitals (mainly $4s$ and $4p$) remaining attached to the Nb core. In order to check whether $4d$ and $5s$ Nb electrons may be indeed con-

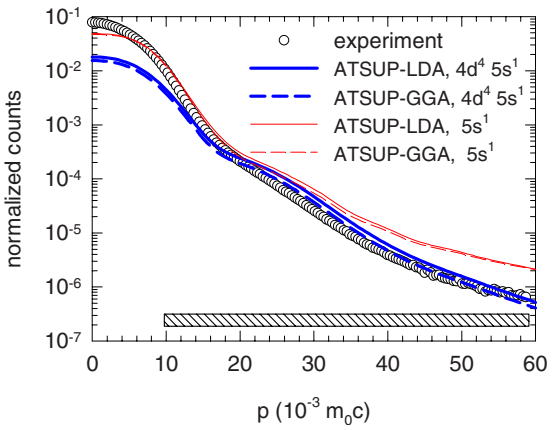

FIG. 15. (Color online) Comparison of experimental CDB profile measured on nonirradiated annealed Nb and HMP curves calculated using ATSUP-LDA (solid lines) and ATSUP-GGA (dashed lines). HMP curves were calculated under two different assumptions: (i) $4d^4$ and $5s^1$ electrons were considered as valence electrons contributing to the low-momentum part of CDB profile (thick lines) and (ii) only $5s^1$ was considered as valence electron, while $4d$ electrons are assumed to be localized in the core orbital state (thin lines). Hatched mark shows the momentum range, where the contribution of the valence electrons may be neglected. A comparison of the calculated HMP curves to experiment is meaningful in this region only.

sidered as low-momentum valence electrons, we examined if there is a significant contribution of $4d$ electrons into the high-momentum region or not. The HMP curves were calculated using two different assumptions:

(i) $4d^4$ and $5s^1$ electrons were treated as valence electrons, i.e., they are assumed to contribute only to the low-momentum part of CDB profile, and

(ii) only $5s^1$ are treated as valence electrons, while $4d^4$ is assumed to be a localized core orbital.

One can see in Fig. 15 that the HMP curve calculated within the assumption (ii) is too high at high momenta. On the other hand, the HMP curve calculated under assumption that *both* $4d^4$ and $5s^1$ are valence electrons and contribute basically to the low-momentum parts of CDB profile is in fairly good agreement with the experimental curve. Thus, the contribution of $4d$ electrons to the high-momentum region of CDB curve ($p > 10 \times 10^{-3}$ m_0c) is rather small. Here we recall that only high-momentum part of the CDB profile can be calculated by ATSUP-based approach. Thus, any comparison to experiment is meaningful only at high momenta where the contribution of core electrons dominates. Figure 15 shows that the HMP curve calculated using the assumption (ii) is in reasonable agreement in the high-momentum region ($p > 10 \times 10^{-3}$ m_0c). Careful analysis of contributions of various orbitals into HMP revealed that a slight difference seen in the momentum range $(20-30) \times 10^{-3}$ m_0c, where the calculated curves are slightly higher than the experimental profile, is due to overestimation of positron-annihilation rate with $3d$ electrons.

The calculated HMP ratio curves, related to that for a defect-free Nb, for vacancy-hydrogen complexes are plotted in Fig. 16. Positions of hydrogen atoms attached to vacancy

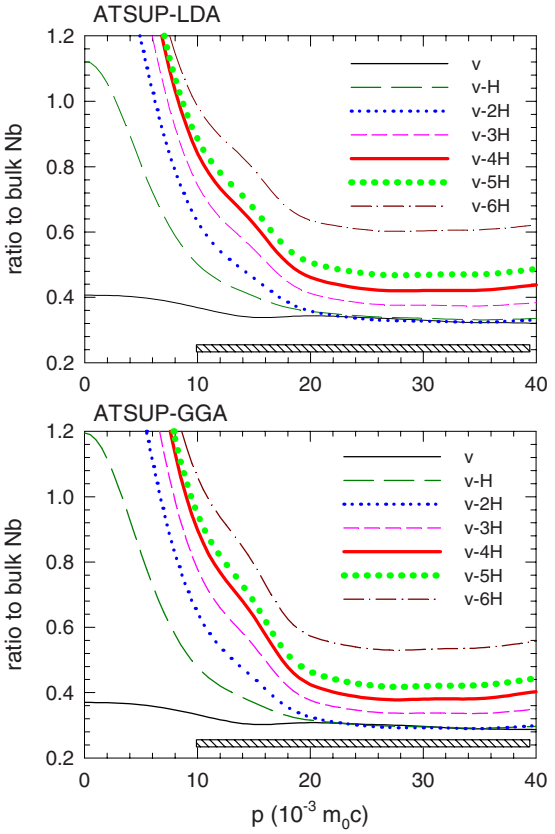

FIG. 16. (Color online) The calculated HMP ratio curves for a nondecorated Nb vacancy (v) and a vacancy surrounded by n H atoms (v-nH). All curves are related to defect-free Nb. Positions of hydrogen atoms attached to vacancy were obtained from EMT calculations in Sec. III B. Upper and lower panels show HMP ratio curves calculated within ATSUP-LDA and ATSUP-GGA approaches, respectively. Hatched mark shows the momentum range, where the contribution of the valence electrons may be neglected.

were obtained from EMT calculations in Sec. III B and HMP curves were calculated within ATSUP-LDA and also ATSUP-GGA schemes. One can see in Fig. 17 that ATSUP-LDA and ATSUP-GGA approaches shown in the upper and lower panels

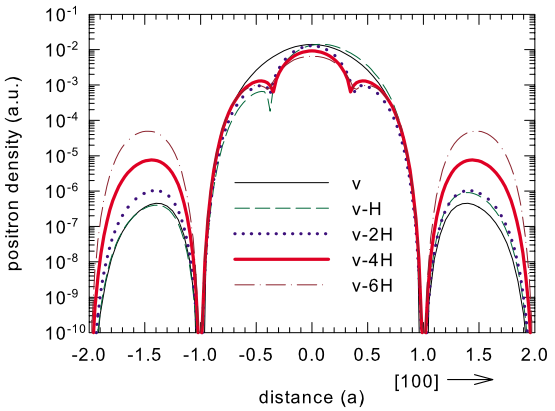

FIG. 17. (Color online) Calculated positron densities in the [100] direction for a nondecorated Nb vacancy (v) and vacancy associated with n H atoms (v-nH). x axis shows length in the units of Nb lattice constant a. Vacancy is located in x=0 position.

in the figure both give very similar pictures. Presence of H attached to a Nb vacancy leads to the appearance of a hump on HMP curves, which is centered at $p \approx 15 \times 10^{-3}\ m_0c$. Interestingly, the HMP curve for a bare Nb vacancy has a slight minimum at $p \approx 15 \times 10^{-3}\ m_0c$, but this feature is reversed by the addition of hydrogen which causes an enhancement of the contribution falling into this momentum range. The hump on HMP curves centered at $p \approx 15 \times 10^{-3}\ m_0c$ clearly becomes more pronounced with increasing number of H atoms surrounding a vacancy. In addition, there is also an overall enhancement of HMP curves in the high-momentum region $p > 20 \times 10^{-3}\ m_0c$ for vacancy-hydrogen complexes. However, the shape of HMP curves at the high-momentum range $p > 20 \times 10^{-3}\ m_0c$ is rather flat without any specific feature, i.e., it has a shape similar to the curve for a nondecorated Nb vacancy. In general one can distinguish the two effects caused by hydrogen atoms attached to a vacancy:

(i) Each hydrogen atom attached to a vacancy introduces an additional electron. In an isolated hydrogen atom this electron is localized in the 1*s* orbital shell. In hydrogen embedded in Nb, this electron interacts with valence Nb electrons. It was shown in Ref. 38 that hybridization of 1*s* electrons with 4*d* band electrons is the most important in Nb.

(ii) Hydrogen attached to a vacancy causes a reduction in positron localization resulting in an enhanced overlap of positron wave function with Nb core electron orbitals. This effect is illustrated in Fig. 17 which shows positron density in the [100] direction calculated for a nondecorated Nb vacancy and for selected vacancy-hydrogen complexes.

Core electrons localized in the inner shells are practically not affected by local environment of Nb ion (frozen-core electrons approximation). Thus, the effect (ii) causes a constant enhancement of HMP ratio curve at high momenta. On the other hand, the electron introduced by hydrogen contributes to the HMP curve specifically at certain momenta. Hence, a hump observed on the calculated HMP ratio curves for vacancy-hydrogen complexes cannot be explained by a decrease of positron localization in defect, but it is rather due to a contribution of positrons annihilated by hydrogen-induced electrons. The presence of a knob at $p \approx 15 \times 10^{-3}\ m_0c$ indicates, therefore, the presence of hydrogen attached to a vacancy.

It is important to mention that our calculations of HMP curves represent only a rough approximation because they are performed for hydrogen electron localized in the 1*s* atomic orbital, i.e., the change of the electron state due to its interaction with Nb valence electrons was not considered. For this reason the agreement of calculated HMP ratio curves with experiment can necessarily be only qualitative. Although the curves plotted in Fig. 16 cannot be used to derive any quantitative conclusions, they are helpful for the interpretation of trends and features observed on the experimental curves.

The experimental CDB ratio curves (related to annealed nonirradiated Nb) measured on the irradiated specimens are plotted in Fig. 18. One can see that the experimental curves exhibit a well pronounced peak at $p \approx 15 \times 10^{-3}\ m_0c$, i.e., at the same position where the calculated HMP curves exhibit a hump. This indicates that positrons annihilated by hydrogen electrons enhance contribution falling into the momentum

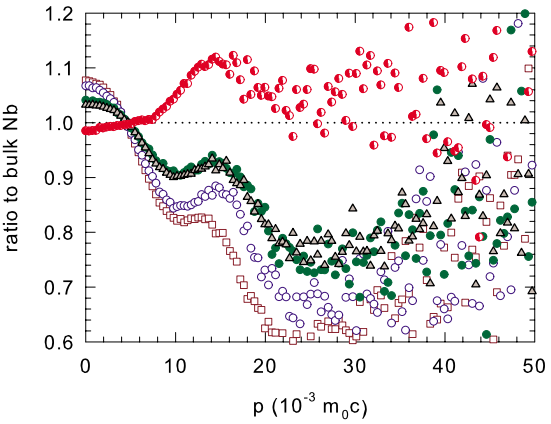

FIG. 18. (Color online) Experimental CDB ratio curves (related to nonirradiated annealed Nb) for the electron-irradiated Nb specimens: open circles—bare Nb irradiated with electrons, full circles—the specimen irradiated with a Pd cap, full triangles—the specimen irradiated with a Cr cap, half-filled circles—the H-loaded specimen. For comparison open squares show the CDB ratio curve for HPT-deformed (nonirradiated) specimen.

range around $15 \times 10^{-3}\ m_0c$, as was predicted by theoretical calculations. Thus, the presence of a peak at $p \approx 15 \times 10^{-3}\ m_0c$ in experimental CDB curves testifies that irradiation-induced vacancies are surrounded by H atoms. Moreover, one can see in Fig. 18 that the "hydrogen peak" at $p \approx 15 \times 10^{-3}\ m_0c$ is enhanced in the specimens irradiated with a Pd (or Cr) cap, where the irradiation-induced vacancies are *on average* surrounded by more H atoms.

One can see in Fig. 18 that in addition to the "hydrogen peak" there is an overall enhancement of the CDB ratio curves at high-momentum range in the specimens irradiated with Pd (or Cr) cap. This is due to a decrease of positron localization in vacancy-hydrogen complex with increasing number of H atoms (cf. Fig. 17) causing an increase in contribution of positrons annihilated by Nb core electrons.

The contribution of delocalized thermalized positron to momentum of the annihilating electron-positron pair is negligible. However, this contribution increases when a positron is spatially confined at a certain defect. In Ref. 56 it was demonstrated that positron trapping at vacancies and dislocations in Al causes the appearance of a well defined peak (centered at $p \approx 8 \times 10^{-3}\ m_0c$) on the CDB ratio curves. This occurs due to non-negligible contribution of positron spatially confined in vacancy (i.e., a region of atomic dimensions) to momentum of the annihilating pair. As the effect of positron localization on the CDB spectrum is relatively similar to the effect of attached hydrogen, it is necessary to estimate shape and magnitude of the contribution originating from positron quantum confinement in Nb vacancies. Momentum density $M_+(\mathbf{p})$ of a positron trapped in a vacancy can be calculated by Fourier transformation of positron wave function

$$M_+(\mathbf{p}) = \left| \int d\mathbf{r} \psi^+(\mathbf{r}) \exp(-\mathbf{ipr}) \right|^2. \qquad (28)$$

The calculated one-dimensional momentum density

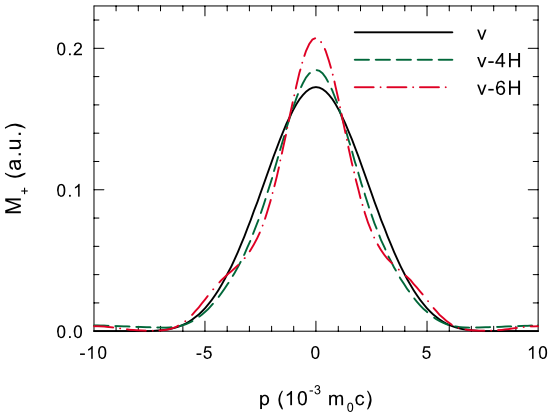

FIG. 19. (Color online) The calculated one-dimensional momentum density for positrons trapped in nondecorated Nb vacancy (solid line), v-4H (dashed line), and v-6H (dash-dotted line) complexes.

$$M_+(p_z) = \int\int dp_x dp_y M_+(\mathbf{p}) \tag{29}$$

of positrons trapped in a nondecorated Nb vacancy, v-4H, and v-6H complexes are plotted in Fig. 19. Note that $p \equiv p_z$ is the momentum component in the direction of measurement. The minimum momentum indetermination of a positron spatially confined over a distance of 2.86 Å (the next neighbor distance in Nb) given by the uncertainty principle amounts to 1.3×10^{-3} m_0c. Increase of positron momentum due to the quantum confinement causes a smearing of Fermi cutoff.[56,57] Positron localization in vacancylike defect provides an enhanced contribution falling in the region above the Fermi momentum and may, therefore, produce a peak in the CDB ratio curves (related to a reference bulk sample). This was clearly demonstrated by Calloni *et al.*[56] on the case of vacancylike defects in Al.

The effect of motion of a confined positron can be studied *separately* by convolution of the calculated momentum distribution of localized positron $M_+(p)$ with electron momentum distribution of an annihilating pair in the perfect bulk material.[56] This way only the effect of positron motion is included, while the effects of reduced electron density and reduced positron-annihilation rate in a vacancy are omitted. In this work we followed the approach used in Ref. 56: the effect of positron confinement was simulated by convolution of the calculated momentum distribution of positron localized in a nondecorated Nb vacancy with momentum distribution $M_b(p)$ corresponding to perfect bulk Nb crystal. Ratio curve $\rho_c(p)$ was constructed by dividing the convoluted distribution by the reference bulk momentum distribution

$$\rho_c(p) = \frac{M_+(p) \star M_b(p)}{M_b(p)}. \tag{30}$$

The momentum distribution $M_b(p)$ for perfect Nb crystal was obtained by two different ways: (i) from experiment, i.e., from CDB measurement of well annealed nonirradiated Nb specimen and (ii) from theoretical calculations. The $M_b(p)$ curve was in the latter case approximated by HMP

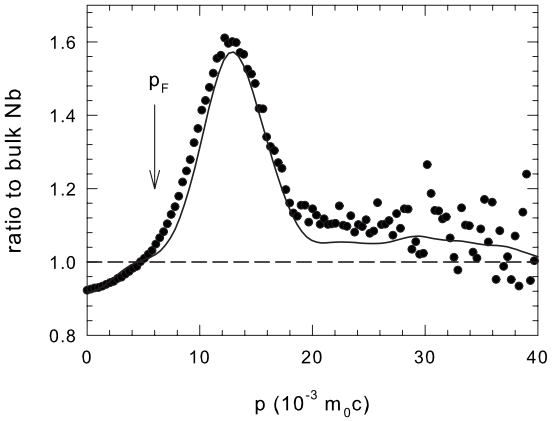

FIG. 20. Ratio curve showing *separately* the effect of positron quantum confinement in a nondecorated Nb vacancy on the CDB ratio curve. The ratio curve was calculated using Eq. (30) with experimental momentum distribution $M_b(p)$ for perfect bulk Nb (full points) and $M_b(p)$ calculated theoretically (solid line). Vertical arrow indicates position of the Fermi momentum.

profile calculated for perfect Nb crystal considering that all electrons are localized in the atomic orbitals. Figure 20 shows the resulting ratio curve ϱ_c simulating the effect of a positron confined in a nondecorated Nb vacancy. One can see in the figure that positron localization caused a peak located at $p \approx 13\times10^{-3}$ m_0c, i.e., at slightly lower momentum than the center of the peak attributed to hydrogen atoms attached to a vacancy (see Fig. 18). The fact that the peak caused by positron localization and the peak caused by trapped hydrogen atoms are relatively closely spaced and overlap each other explains why just a singe peak is visible on the CDB ratio curves measured on irradiated and hydrogen-loaded specimens plotted in Fig. 18.

Magnitude of the peak originating from positron localization cannot be determined from Fig. 20 because it does not include reduction of electron density and positron-annihilation rate in a vacancy. Therefore, we determined the magnitude of this effect experimentally using the HPT-deformed Nb specimen. The LT measurements described in Sec. IV D revealed that HPT-deformed Nb exhibits a high density of dislocations and more than 90% of positrons annihilate in vacancies anchored in the elastic field of dislocations. Hence, HPT-deformed specimen represents a material where most of the positrons are trapped at vacancylike defects. However, contrary to electron-irradiated specimens these vacancylike defects are not decorated by hydrogen and the CDB ratio curve shows, therefore, the effect of positron localization only. One can see that the CDB ratio curve of the HPT-deformed specimen, which is plotted in Fig. 18, exhibits indeed a peak located close to $p \approx 13\times10^{-3}$ m_0c as predicted by theory. It is clearly seen in Fig. 18 that this peak caused by positron localization in HPT-deformed Nb is located at lower momenta compared to the peaks observed at irradiated and hydrogen-loaded specimens.

Thus, one can conclude that positron localization in vacancylike defects in Nb causes a measurable effect and cannot be neglected in interpretation of CDB results. On the other hand, the peaks observed in irradiated and hydrogen-

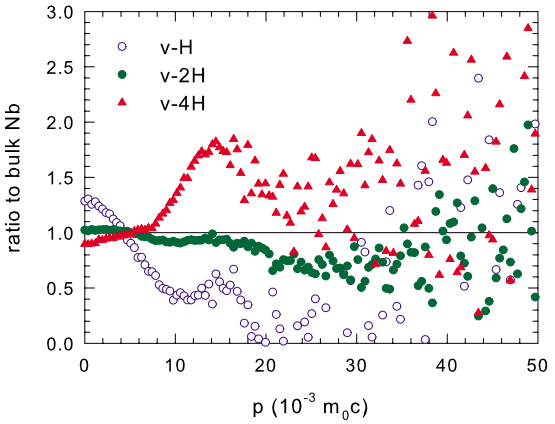

FIG. 21. (Color online) CDB ratio curves for v-H, v-2H, and v-4H complexes. Curves were calculated using Eq. (31).

loaded specimens cannot be explained by quantum confinement of positron in vacancy for several reasons:

(i) The magnitude of the peak caused by positron localization in a vacancy is remarkably lower than the peak centered at $p \approx 15 \times 10^{-3}$ m_0c observed on the CDB ratio curves of irradiated and hydrogen-loaded specimens.

(ii) The peak caused by positron localization is located at slightly lower momenta than the peak caused by hydrogen.

(iii) The peak located at $p \approx 15 \times 10^{-3}$ m_0c increases with increasing number of H atoms surrounding a vacancy, i.e., with decreasing positron localization, while the peak caused by quantum confinement should exhibit opposite behavior because momentum distribution of confined positron becomes narrower with increasing number of H atoms decorating a vacancy.

The CDB ratio curve $\rho(p)$ measured on the irradiated specimens is a superposition of three contributions: (i) free (delocalized) positrons, (ii) positrons trapped at v-H, and (iii) positrons trapped at v-2H complexes

$$\rho(p) = f_0 + \rho_{v\text{-H}}(p) f_{v\text{-H}} + \rho_{v\text{-2H}}(p) f_{v\text{-2H}}. \tag{31}$$

The notations $\rho_{v\text{-H}}$ and $\rho_{v\text{-2H}}$, respectively, represent CDB ratio curves for v-H and v-2H complexes, i.e., curves for 100% contribution of positrons annihilated in the corresponding complexes, and $f_{v\text{-H}}$ and $f_{v\text{-2H}}$ are fractions of positrons annihilated at these complexes. The CDB ratio curves $\rho_{v\text{-H}}$ and $\rho_{v\text{-2H}}$ can be determined by applying Eq. (31) on the CDB profiles measured on the irradiated specimens and using the positron fractions calculated from LT results (Table IV) by Eqs. (22) and (23). The resulting CDB ratio curves $\rho_{v\text{-H}}$ and $\rho_{v\text{-2H}}$ for v-H and v-2H complexes, respectively, are plotted in Fig. 21. The $\rho_{v\text{-2H}}$ curve is more similar to that for bulk Nb compared to the curve for v-H complexes. It is in agreement with the fact that the point corresponding to v-2H complexes in the S-W plot (Fig. 13) is located relatively close to that for bulk Nb.

The experimental CDB ratio curve for the specimen irradiated with Pd cap and subsequently electrochemically loaded with hydrogen is plotted in Fig. 18 as well. One can see that the H-loaded specimen exhibits substantially enhanced contribution in the high-momentum range, which becomes even higher than in the well-annealed (defect-free) Nb specimen. Moreover, the peak at $p \approx 15 \times 10^{-3}$ m_0c, which is related to hydrogen, is significantly higher than in the specimens irradiated only, but not charged with hydrogen. These features seen on the CDB curve are in concordance with enhanced number of H atoms surrounding vacancies in the loaded specimen. While the irradiated specimens contain a mixture of v-H and v-2H complexes, the H-loaded specimen contains exclusively v-4H complexes (see Sec. IV C). Similarly to Eq. (31), the CDB ratio curve measured on the H-loaded specimen can be expressed as a superposition of two contributions: (i) free (delocalized) positrons and (ii) positrons trapped at v-4H complexes

$$\rho(p) = (1 - f_{v\text{-4H}}) + \rho_{v\text{-4H}}(p) f_{v\text{-4H}}. \tag{32}$$

Here $\rho_{v\text{-4H}}$ is the CDB ratio curve for v-4H complexes, i.e., a 100% contribution of positrons annihilating from a trapped state at v-4H complexes. The ratio curve $\rho_{v\text{-4H}}$ derived from Eq. (32) using the fraction $f_{v\text{-4H}}$ calculated from the LT results in Table II is plotted in Fig. 21. The $\rho_{v\text{-4H}}$ curve exhibits a remarkably enhanced high-momentum part compared to v-H and v-2H complexes and a pronounced peak centered at $p \approx 15 \times 10^{-3}$ m_0c. On the other hand, the low-momentum part of this curve is lowered. This shows clearly the effect of increasing number of H atoms surrounding a vacancy, i.e., (i) an enhanced fraction of positrons annihilated by hydrogen electrons contributing into the "hydrogen peak" at $p \approx 15 \times 10^{-3}$ m_0c and (ii) a decrease of the open volume in vacancy which leads to a reduced localization of positron wave function illustrated in Fig. 17 and causes an overall increase of the CDB profile in the high-momentum range.

V. CONCLUSIONS

Nb specimens irradiated by 10 MeV electrons were investigated in this work. It was found that vacancies introduced into Nb by electron irradiation are surrounded by H atoms. The irradiated Nb specimens contain a mixture of v-H and v-2H complexes. The v-2H complexes represent a predominant type of defects in all irradiated specimens. The specimens irradiated with Pd (or Cr) cap contain a higher relative fraction of v-2H complexes. When the irradiated specimens are electrochemically doped with hydrogen, i.e., more hydrogen is introduced into the specimens, the v-H and v-2H complexes are transformed into v-4H complexes. It has been demonstrated that a H atom attached to a vacancy can be identified by CDB. The obtained results also demonstrate that PAS can be used to determine the hydrogen content in the irradiated specimens within a ppm precision, which is impossible to achieve with standard XRD.

ACKNOWLEDGMENTS

The authors are grateful to Jan Kuriplach (Charles University in Prague) for providing them with the ATSUP code. Financial support from the Ministry of Education of The Czech Republic (Project No. MS 0021620834) and the Alexander von Humboldt Foundation are highly acknowledged.

*jakub.cizek@mff.cuni.cz

[1] H. Schultz, in *Point Defects and Defect Interactions in Metals*, edited by J. Takamura, M. Doyama, and M. Kiritani (University of Tokyo Press, Tokyo, 1982), p. 183.
[2] J. Völkl and G. Alefeld, in *Hydrogen in Metals I*, edited by G. Alefeld and J. Völkl, Topics in Applied Physics Vol. 28 (Springer-Verlag, Berlin, 1978), p. 321.
[3] P. Kesten, A. Pundt, G. Schmitz, M. Weisheit, H. U. Krebs, and R. Kirchheim, J. Alloys Compd. **330-332**, 225 (2002).
[4] A. Pundt and R. Kirchheim, Annu. Rev. Mater. Res. **36**, 555 (2006).
[5] P. Hautojärvi, in *Positrons in Solids*, edited by P. Hautojärvi (Springer-Verlag, Berlin, 1979), p. 1.
[6] B. Lengeler, S. Mantl, and W. Triftshäuser, J. Phys. F: Met. Phys. **8**, 1691 (1978).
[7] P. Hautojärvi, L. Pöllänen, A. Vehanen, and J. Yli-Kauppila, J. Nucl. Mater. **114**, 250 (1983).
[8] P. Hautojärvi, H. Huomo, M. Puska, and A. Vehanen, Phys. Rev. B **32**, 4326 (1985).
[9] J. Čížek, I. Procházka, F. Bečvář, R. Kužel, M. Cieslar, G. Brauer, W. Anwand, R. Kirchheim, and A. Pundt, Phys. Rev. B **69**, 224106 (2004).
[10] R. Valiev, R. Islamgaliev, and I. Alexandrov, Prog. Mater. Sci. **45**, 103 (2000).
[11] F. Bečvář, J. Čížek, L. Lešták, I. Novotný, I. Procházka, and F. Šebesta, Nucl. Instrum. Methods Phys. Res. A **443**, 557 (2000).
[12] F. Bečvář, J. Čížek, and I. Procházka, Acta Phys. Pol. A **95**, 448 (1999).
[13] I. Procházka, I. Novotný, and F. Bečvář, Mater. Sci. Forum **255-257**, 772 (1997).
[14] J. Čížek, I. Procházka, B. Smola, I. Stulíková, R. Kužel, Z. Matěj, and V. Cherkaska, Phys. Status Solidi A **203**, 466 (2006).
[15] W. Anwand, H.-R. Kissener, and G. Brauer, Acta Phys. Pol. A **88**, 7 (1995).
[16] A. van Veen, H. Schut, M. Clement, J. M. M. de Nijs, A. Kruseman, and M. IJpma, Appl. Surf. Sci. **85**, 216 (1995).
[17] M. J. Puska and R. M. Nieminen, Rev. Mod. Phys. **66**, 841 (1994).
[18] E. Boroński and R. M. Nieminen, Phys. Rev. B **34**, 3820 (1986).
[19] M. J. Puska and R. M. Nieminen, J. Phys. F: Met. Phys. **13**, 333 (1983).
[20] J. P. Desclaux, Comput. Phys. Commun. **1**, 216 (1970).
[21] J. P. Desclaux, Comput. Phys. Commun. **9**, 31 (1975).
[22] G. Kresse and J. Hafner, Phys. Rev. B **47**, 558 (1993).
[23] G. Kresse and J. Furthmüller, Phys. Rev. B **54**, 11169 (1996).
[24] G. Kresse and J. Furthmüller, Comput. Mater. Sci. **6**, 15 (1996).
[25] J. Arponen and E. Pajane, Ann. Phys. (N.Y.) **121**, 343 (1979).
[26] B. Barbiellini, M. J. Puska, T. Korhonen, A. Harju, T. Torsti, and R. M. Nieminen, Phys. Rev. B **53**, 16201 (1996).
[27] B. Barbiellini, M. J. Puska, T. Torsti, and R. M. Nieminen, Phys. Rev. B **51**, 7341 (1995).
[28] T. Korhonen, M. J. Puska, and R. M. Nieminen, Phys. Rev. B **54**, 15016 (1996).
[29] J. C. Robles, E. Ogando, and F. Plazaola, J. Phys.: Condens. Matter **19**, 176222 (2007).
[30] M. J. Puska, A. P. Seitsonen, and R. M. Nieminen, Phys. Rev. B **52**, 10947 (1995).
[31] I. Makkonen, M. Hakala, and M. J. Puska, Phys. Rev. B **73**, 035103 (2006).
[32] P. E. Blöchl, Phys. Rev. B **50**, 17953 (1994).
[33] M. Alatalo, B. Barbiellini, M. Hakala, H. Kauppinen, T. Korhonen, M. J. Puska, K. Saarinen, P. Hautojärvi, and R. M. Nieminen, Phys. Rev. B **54**, 2397 (1996).
[34] J. Kuriplach, A. L. Morales, C. Dauwe, D. Segers, and M. Šob, Phys. Rev. B **58**, 10475 (1998).
[35] H. Peisl, in *Hydrogen in Metals I*, edited by G. Alefeld and J. Völkl, Topics in Applied Physics Vol. 28 (Springer-Verlag, Berlin, 1978), p. 53.
[36] D. Larsen and J. Nørskov, J. Phys. F: Met. Phys. **9**, 1975 (1979).
[37] M. Baskes and C. Melius, Z. Phys. Chem., Neue Folge **116**, 289 (1979).
[38] J. K. Nørskov, Phys. Rev. B **26**, 2875 (1982).
[39] M. J. Stott and E. Zaremba, Phys. Rev. B **22**, 1564 (1980).
[40] J. K. Nørskov, Phys. Rev. Lett. **48**, 1620 (1982).
[41] J. K. Nørskov, F. Besenbacher, J. Bøttiger, B. B. Nielsen, and A. A. Pisarev, Phys. Rev. Lett. **49**, 1420 (1982).
[42] W. Schilling, J. Nucl. Mater. **69**, 1977 (1977).
[43] S. T. Picraux, Nucl. Instrum. Methods **182-183**, 413 (1981).
[44] S. M. Myers, S. T. Picraux, and R. E. Stoltz, J. Appl. Phys. **50**, 5710 (1979).
[45] M. Berger, J. S. Coursey, M. A. Zucker, and J. Chang, ESTAR, PSTAR, and ASTAR: Computer Programs for Calculating Stopping-Power and Range Tables for Electrons, Protons, and Helium Ions (Version 1.2.3), National Institute of Standards and Technology, Gaithersburg, 2005 (http://physics.nist.gov/Star).
[46] ICDD (International Centre for Diffraction Data), powder-diffraction pattern database, PDF-2.
[47] A. Vehanen and Y. Rytsola, in *Positron Solid-State Physics*, edited by W. Brandt and A. Dupasquier (North-Holland, Amsterdam, 1983), p. 668.
[48] R. West, in *Positrons in Solids*, edited by P. Hautojärvi (Springer-Verlag, Berlin, 1979), p. 89.
[49] P. Hautojärvi, H. Huomo, P. Saariaho, A. Vehanen, and J. Yli-Kauppila, J. Phys. F: Met. Phys. **13**, 1415 (1983).
[50] L. Smedskjaer, M. Manninen, and M. Fluss, J. Phys. F: Met. Phys. **10**, 2237 (1980).
[51] J. Čížek, I. Procházka, M. Cieslar, R. Kužel, J. Kuriplach, F. Chmelík, I. Stulíková, F. Bečvář, O. Melikhova, and R. K. Islamgaliev, Phys. Rev. B **65**, 094106 (2002).
[52] A. Vehanen, P. Hautojärvi, J. Johansson, J. Yli-Kauppila, and P. Moser, Phys. Rev. B **25**, 762 (1982).
[53] R. M. Nieminen and J. Laakkonen, Appl. Phys. (Berlin) **20**, 181 (1979).
[54] M. A. Pick, J. W. Davenport, M. Strongin, and G. J. Dienes, Phys. Rev. Lett. **43**, 286 (1979).
[55] M. Venkatraman and J. Neumann, in *Phase Diagrams of Binary Hydrogen Alloys*, edited by F. Manchester (ASM International, Materials Park, 2000), p. 37.
[56] A. Calloni, A. Dupasquier, R. Ferragut, P. Folegati, M. M. Iglesias, I. Makkonen, and M. J. Puska, Phys. Rev. B **72**, 054112 (2005).
[57] S. Berko and J. C. Erskine, Phys. Rev. Lett. **19**, 307 (1967).